

**The National Nanotechnology  
Infrastructure Network**

**Research Experience  
for Undergraduates  
(NNIN REU) Program**

**2009  
Research  
Accomplishments**

# Role of Reactive Oxygen Species in Nanotoxicity

Sarah Connolly

Biochemistry/Microbiology, University of Florida

**NNIN REU Site: Nanofabrication Center, University of Minnesota-Twin Cities, Minneapolis, MN**

*NNIN REU Principal Investigator(s): Dr. Christy Haynes, Chemistry, University of Minnesota*

*NNIN REU Mentor(s): Melissa Maurer-Jones, Chemistry, University of Minnesota*

*Contact: sarahsconnolly@ufl.edu, chaynes@umn.edu, jone1317@umn.edu*

## **Abstract:**

Though the emergence of the nanotechnology field has increased the incorporation of nanomaterials into commercially available products, we have limited understanding of how its widespread applications can affect us personally. This project focused on observing the presence of reactive oxygen species (ROS) in mouse fibroblast model cells when exposed to nano-titanium dioxide (nTiO<sub>2</sub>) utilizing various fluorescent probe assays including 4-((9-acridinecarbonyl) amino)-2,2,6,6-tetramethylpiperidin-1-oxyl (TEMPO-9-AC) and 2',7'-dichlorodihydrofluorescein diacetate (H<sub>2</sub>DCFDA). ROS can cause oxidative stress in cells, which may lead to cell dysfunction, mutation, or death. Cellular uptake of the nanoparticles was studied using inductively coupled plasma-atomic emission spectroscopy (ICP-AES) analysis to correlate ROS generation with cellular internalization of nTiO<sub>2</sub>, followed by a commonly used cellular viability assay which showed insignificant difference in cell viability; the elevated uptake and increased ROS levels may have harmful effects on cell function of living cells.

## **Experimental Procedure:**

Anatase titanium dioxide nanoparticles were made by a sol-gel synthesis using isopropyl alcohol and titanium isopropoxide that were stirred and chilled for 30 minutes while a nitric acid catalyst was added; then the mixture was refluxed for 24 hours. Samples were dialyzed over a 5-10 day period followed by aging in an acid digestion bomb for 48 hours in a 200°C oven. Finally, the aged nanoparticle suspension was washed with ethyl alcohol and dried [1]. Nanoparticles were characterized using x-ray diffraction to determine their crystalline structure, dynamic light scattering to determine particle aggregation, and transmission electron microscopy to determine particle size.

ICP-AES was performed to quantify the number of nanoparticles internalized by cells after incubation with nTiO<sub>2</sub> at a concentration of 100 µg/ml for 24, 48, and 72 hours. Cells were rinsed three times with PBS and removed from the Petri® dish using trypsin enzyme. The Petri dish was scraped and the trypsin-cell suspension was put in a centrifuge tube with 1 mL of 2:1 H<sub>2</sub>SO<sub>4</sub>:HNO<sub>3</sub> digest solution in 3 mL H<sub>2</sub>O and sonicated for one hour.

For the fluorescent assays, 3T3 mouse fibroblasts were plated in a clear bottom 96-well plate at a density of 10<sup>4</sup>-10<sup>5</sup> cells/well and exposed to the fluorescent probe. TEMPO detects superoxide and hydroxyl radical while H<sub>2</sub>DCFDA detects superoxide, hydroxyl radical, peroxy radical, and singlet oxygen. After a one hour incubation period with the fluorescent probe, the probe was removed and the cells were rinsed once with PBS. Cells were then exposed to nTiO<sub>2</sub> at various concentrations (12.5, 25, 50, 100, 200, and 400 µg/ml)

for 24 and 48 hours. For the positive controls, malachite green—a superoxide and hydroxyl radical generator, and rose bengal—a singlet oxygen generator, were used. After incubation, the nTiO<sub>2</sub> and media were removed, cells rinsed twice with PBS, and a uniform volume of PBS added to each well. Fluorescence intensity was then measured with a fluorescent plate reader.

An MTT (3-(4,5-dimethylthiazol-2-yl)-2,5-diphenyltetrazolium bromide) assay was performed in 24 well plates to assess cell viability. 3T3 cells were again incubated with the various concentrations of nTiO<sub>2</sub> listed above, for 24, 48, and 72 hours. Following incubation, the media and nTiO<sub>2</sub> were removed, cells rinsed three times with PBS, and incubated with MTT in cell media for two hours. The MTT was removed and DMSO was added to each well to dissolve the formazan crystals. After 20 minutes, optical density was measured at λ = 570 nm, and the absorbance was correlated to the percentage of viable cells.

## **Results and Conclusions:**

Results from ICP analysis (Figure 1) show that the longer the cells were exposed to nTiO<sub>2</sub>, the more nanoparticles the cells internalized. We hypothesized that longer incubation time, and more cellular internalization of nTiO<sub>2</sub>, would lead to more ROS generation.

Linear regression analysis of our fluorescent probe assays (Figures 2 and 3) showed that there was a significant

increase in ROS as the concentration of nTiO<sub>2</sub> increased, leading us to assume greater oxidative stress on the cell and to hypothesize that this would lead to a decrease in cellular viability. However, statistical analysis (by student t-testing) shows that there is no significant difference between 24 and 48 hour incubation times, meaning that our previous hypothesis about longer incubation correlating to increased ROS production is false. In the future, we would like to extend incubation times past 48 hours, as this might show a more obvious trend.

Results from the cell viability assay (Figure 4) show statistically insignificant change in cell viability. This means that the increased concentration of nTiO<sub>2</sub>, as well as varying exposure times, is not killing the cells, negating our hypothesis.

**Future Work:**

We would like to compare these results to those of similar assays performed on the immortalized mast cell line rat basophilic leukemia (RBL) cells. Mast cells play a critical role in immune response, and thus are an interesting, relevant cell for nanotoxicity studies.

Amperometry studies are currently underway to determine the effects of ROS on cell exocytosis. The results of these experiments will allow us to make predictions about overall cell health and function due to the internalization of nTiO<sub>2</sub> and increased amounts of ROS generated.

**Acknowledgements:**

I would like to thank Dr. Christy Haynes, Melissa Maurer-Jones, and the Haynes Research Group for kindly sharing

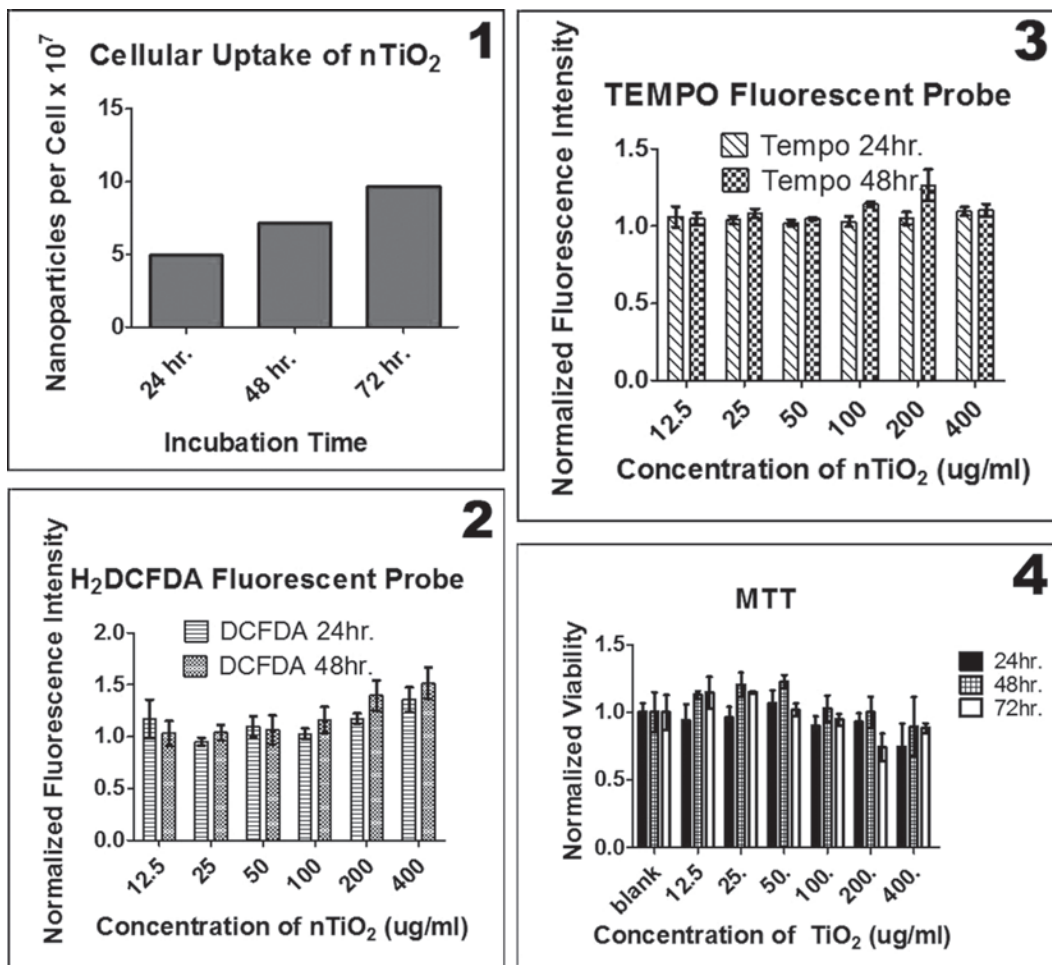


Figure 1: Cellular internalization of nTiO<sub>2</sub> increases with incubation time.

Figure 2: Increase in fluorescence intensity indicates an increase in ROS production as nTiO<sub>2</sub> concentration increases.

Figure 3: Linear regression analysis shows significant increase in fluorescence intensity as nTiO<sub>2</sub> concentration increases.

Figure 4: There is no significant decrease in cell viability over time or as concentration of nTiO<sub>2</sub> increases.

their lab with me and patiently mentoring me. Also, I would like to thank Dr. Doug Ernie, Dr. Bruce Wollenberg, Becky von Dissen, Brooke Myhre, and Melanie-Claire Mallison for their time spent organizing this REU program. Finally, I would like to thank the National Nanotechnology Infrastructure Network Research Experience for Undergraduates Program for this opportunity and the National Science Foundation for funding.

**References:**

[1] Titanium Dioxide Nanoparticles: Effect of Sol-Gel pH on Phase Composition, Particle Size, and Particle Growth Mechanism, S. L. Isley and R. L. Penn (2008), Journal of Physical Chemistry C, 112, 4469-4474.

# Microfluidic Single-Cell Assay Chip for Drug Efficacy Test

Nicolas Andrew Shillingford-Cordero  
 Microbiology, Cornell University

**NNIN REU Site:** Lurie Nanofabrication Facility, University of Michigan, Ann Arbor, MI  
**NNIN REU Principal Investigator(s):** Euisik Yoon, Electrical Engineering, University of Michigan  
**NNIN REU Mentor(s):** Xia Lou, Electrical Engineering, University of Michigan  
**Contact:** nac56@cornell.edu, esyoon@umich.edu, xialou@umich.edu

## Abstract:

Single-cell resolution assays incomparably increase the power of drug screens over conventional colorimetric assays by providing quantitative data. Assays of this class avoid cell-to-cell interactions present in traditional bulk sampling procedures; these interactions can mask nuances where individual cells are concerned, invariably causing rich amounts of information to be overlooked. Advances in microfluidic technology have allowed high throughput single-cell drug screens to be performed while exercising precise control over cell loading and culturing conditions with relatively insignificant amounts of expensive samples and reagents used. This project focused on optimizing the design and operation of our drug screening platform for single-cells and neurospheres. Microfluidic chips were fabricated via polydimethylsiloxane (PDMS) replication and bonding. Glioblastoma multiforme (GBM) cells—stained with green fluorescent protein (GFP)—were then introduced to the devices and, upon their capture within individual microwells, cultured to the neurosphere stage while being subjected to drug screens alongside control groups. Significant statistical data of cell viability can be obtained when the starting single-cell number in the chip is greater than 100 and after these cells have been cultured in the chip for at least five days.

## Introduction:

Cell-based biological assays, such as drug screens, are notorious for frequently providing the mean data across an entire population of cells, despite the now ubiquitous knowledge that isolated cells, even those belonging to related cell lines, portray extremely diverse properties [1]. Advancements in microfluidic single-cell assay technologies provide biologists with a media through which they can tackle the most adamant challenges.

The quest for finding the cure to cancer is as much a race against time as it is against money, but by utilizing the properties of microfluidic PDMS chips the burden on humanity and on its coffers can be significantly reduced. These inexpensive chips can be used to segregate cells into discrete compartments, allowing many types of quantitative assays to be performed. This project focuses on optimizing the design and operation of a microfluidic single-cell drug screening platform for GBM cells.

Currently, GBM is the most common type of primary brain tumor and only palliative treatments exist. With this design, it is possible to culture single GBM cells to the neurosphere stage, allowing drug screens to account for the aging of cells, something previously unaccomplished. This design further prevents cell-to-cell interactions by providing a constant flow of fresh medium over the cells.

**Microfluidic Chip Fabrication and Preparation.** Photolithography of SU-8 on silicon wafers was used to create

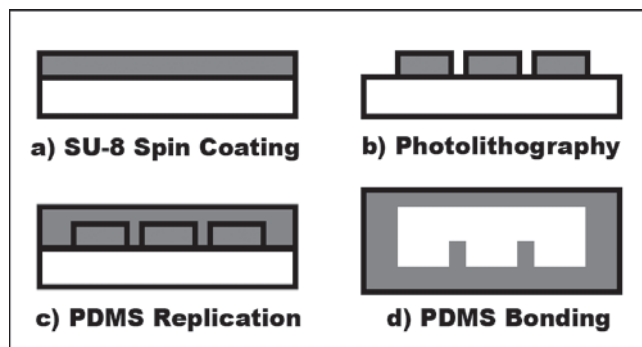


Figure 1, top: Microfluidic PDMS chip fabrication.  
 Figure 2, bottom: Microfluidic PDMS chip.

master molds for the channel (top) and microwell (bottom) halves of the PDMS chips (Figure 1). Input and output holes were punched into the channel half of a PDMS chip and then the two halves were treated with oxygen plasma and bonded (Figure 2). Cell-free medium was inserted at the input (80  $\mu\text{L}$ ) and output (40  $\mu\text{L}$ ) wells of the chip which was then degassed in a vacuum chamber to flush air bubbles from the channels.

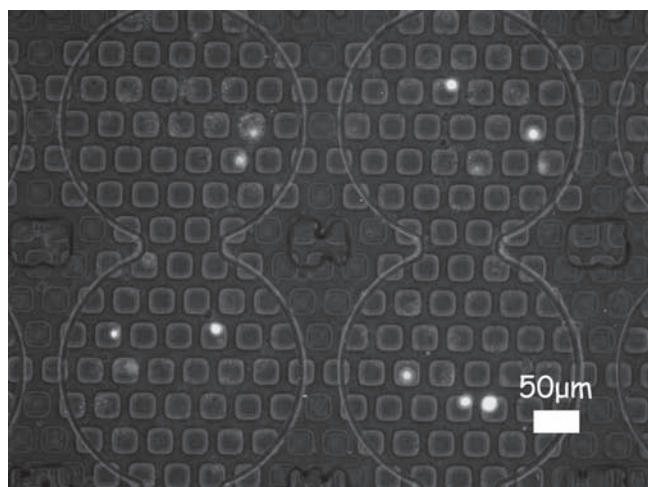


Figure 3: GBM single-cells.

**Cell-Loading Procedure.** The GBM neurospheres in the cell-containing medium were then manually disassociated to single-cells using a micropipette. The cell-free medium was removed from the input and output wells of the chip; cell-containing medium (80  $\mu\text{L}$ ) was then inserted at the input well. The medium was allowed to flow for 10 minutes before being removed from both wells; the cells in the microfluidic chip were allowed to settle for three minutes. The chip was then inspected with ultraviolet light (10X magnification) for neurospheres stuck in the channels, which were removed by providing negative pressure at the output well via pipette bubble suction. The single-cell captures were then counted manually (Figure 3). If the chip contained less than 100 single-cell captures, more cell-containing medium (80  $\mu\text{L}$ ) was inserted at the input well and the process was repeated until at least 100 cells were captured.

**Drug Screening.** Once 100 cells were captured, the cells were subjected to drug screens. For the control group, cell-free medium (80  $\mu\text{L}$ ) was injected into the inlets and the cells were cultured for more than five days while being subjected to a continuous flow of fresh medium from inlet to outlet via gravity difference. Chips were kept in an incubator set at 37°C, 5% CO<sub>2</sub> and 90% RH; fresh medium was replaced and cell viability recorded via GFP staining every 12 hours. For the treatment group, cell-free medium containing the drug (GSI) was used instead. Statistics were obtained for cell viability.

## Results and Discussion:

The cell-loading procedure was first optimized using microbeads (15  $\mu\text{m}$ ) of similar size to GBM cells (Figure 4). The microbeads were most efficiently captured with the following: channel height, 22  $\mu\text{m}$ ; microwell diameter, 20  $\mu\text{m}$ , microwell depth, 26  $\mu\text{m}$ ; bead concentration,  $2.75 \times 10^6$  beads/mL. For the GBM cells, slight dimensional tweaking was required to compensate for the cells' affinity to each other: channel height, 37  $\mu\text{m}$ ; microwell diameter, 30  $\mu\text{m}$ ; microwell depth, 26  $\mu\text{m}$ . As in the microbead experiments, the cell-loading procedure was most efficient when a high concentration of cells (greater than  $10^6$  cells/mL) was used, with which capturing over 100 cells became trivial. Preliminary drug screenings were unsuccessful at distinguishing a significant difference between viability in control (34.74%) and treatment group cells (34.84%). More frequent medium changes may be necessary for future screenings.

## Acknowledgements:

Infinite gratitude goes to Professor Euisik Yoon and his research group for taking me as an intern and to Xia Lou for the fantastic mentoring that will be forever useful in future endeavors. Great thanks to Dr. Tom Bersano for his assistance with the cell-loading procedure. Much appreciation to the National Nanotechnology Infrastructure Network Research Undergraduate Experience Program, the National Science Foundation, and the wonderful staff at the Lurie Nanofabrication Facility for giving this biologist a taste of engineering.

## References:

- [1] Sims, C. E., and N. L. Allbritton. "Analysis of single mammalian cells on-chip". *Lab on a Chip*, 7, 423-440 (2007).

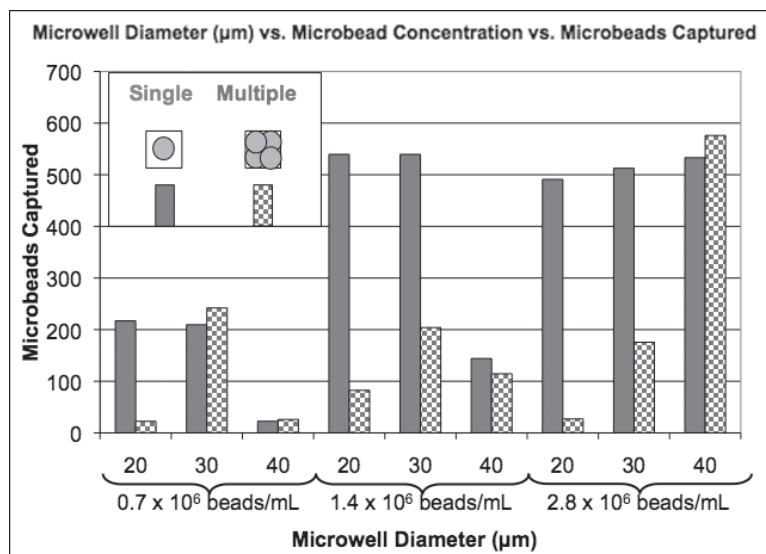


Figure 4: Optimization of microbead capture.

# Nanotextured Surfaces: New Generation Bioelectronic Interfaces for Nanomedicine

Ericka Cottman

Electrical Engineering, Virginia Commonwealth University

NNIN REU Site: ASU NanoFab, Arizona State University, Tempe, AZ

NNIN REU Principal Investigator(s): Dr. Jennifer Blain Christen, Electrical Engineering, Arizona State University

NNIN REU Mentor(s): David Welch, BioEngineering, Arizona State University

Contact: cottmaner@vcu.edu, jennifer.blainchristen@asu.edu, djwelch1@asu.edu

## Abstract:

Bioelectronics is a field of study that contributes to a growing intersection between nanostructures and nanomedicine. One application is using nanostructures for interfacing cells. This can help improve standard signal measurements from cells on a two-dimensional electrode array by using a nanotextured electrode surface instead. Nanotexturing increases the surface area to improve the adhesion of cells to electrodes and provides a more efficient electrical interface. We used a porous alumina membrane as a template to provide uniform nano-scale pores for electrodeposition of gold onto two-dimensional arrays of gold electrodes. We performed extensive characterization of electrodeposition parameters including, current density, deposition rate, nanorod uniformity, and experimental repeatability. Finally, we cultured HL-1 cardiomyocytes on the nanotextured gold arrays and characterized morphology, adhesion, and proliferation rate. These experiments confirmed our ability to culture electrically active cells on nanotextured gold electrodes.

## Experimental Procedure:

We fabricated two-dimensional electrode arrays for nanotexturing using standard microfabrication techniques. The lithography was performed on glass substrates using a mask with electrodes and wires leading to bond pads. A 10 nm adhesion layer of chrome was deposited on the glass followed by a 100 nm layer of gold with the Edwards #2 thermal evaporator. Lift-off, agitating the substrate in acetone, patterned the chrome and gold.

The gold electrode array was modified using electrodeposition. Our experimental setup is illustrated in Figure 2. The electrical parameters for the deposition were controlled using a potentiostat. We built this circuit on a proto-board using two operational amplifiers, a resistor, and three electrodes operated using a power supply and a computer-controlled source measurement unit [1]. The potentiostat is used to monitor and control electrochemical reactions utilizing three electrodes. The counter electrode (CE) is used to apply a current, the reference electrode (RE) gives the solution a “chemical ground” and the working electrode (WE) allows for current flow. The counter and reference electrodes go into the solution, but they can be shorted together since they are at the same potential. The working electrode makes electrical contact with the bond pads on the patterned gold substrate. The glass slide patterned with gold was placed in between the two Teflon® cylinders, the top one containing CE, RE, and the ionic solution; this completes the circuit allowing current to flow. The electrodeposition performed with this setup is an electrochemical method for driving gold cations toward an electrode in solution. Potassium aurocyanide ( $\text{KAu}(\text{CN})_2$ ) was the gold ion solution placed in the electrochemical cell. Within the solution, the current

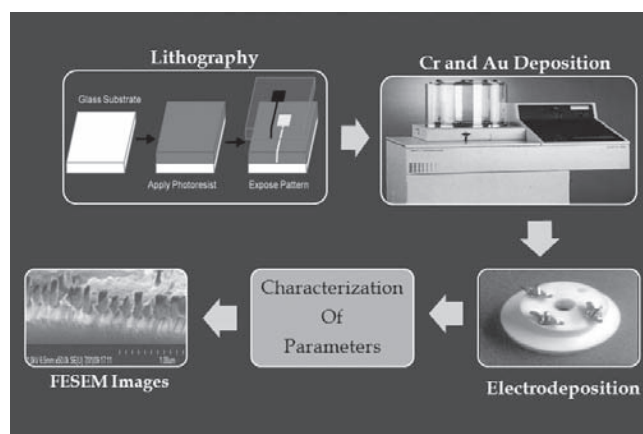
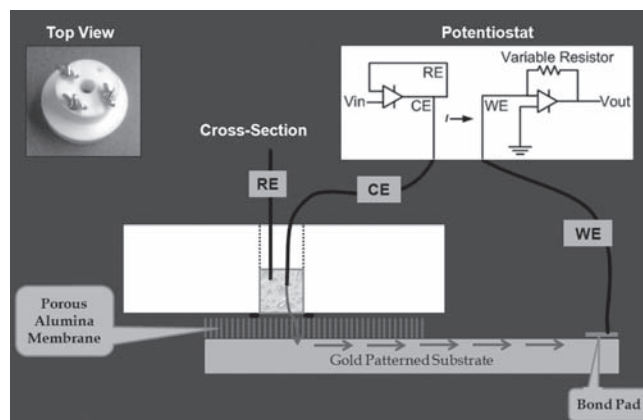


Figure 1, above: Process overview: lithography, deposition, electrodeposition, parameters characterized, and FESEM images.

Figure 2, below: Electrodeposition experimental setup includes: potentiostat circuit, three electrodes, membrane on patterned gold substrate, and potassium aurocyanide.



flow described is the movement of gold cations toward the patterned gold electrodes forming the deposited gold.

A porous alumina membrane was used as a template for the nanorod growth. The membrane is 40  $\mu\text{m}$  thick and has pores with a 200 nanometer diameter. When placed above the electrode array as shown in the Figure 2, the flow of cations was restricted to the pore interior. Current flows through the pores of membrane then to the electrodes, resulting in the precipitation of gold within the pores. This results in the deposition of the 200 nm diameter gold rods with thickness depending on experimental parameters. This creates free-standing gold rods once the membrane is dissolved with sodium hydroxide.

### **Results and Conclusion:**

One of our goals for this research was to correlate many experimental parameters with the resulting nanorod growth characteristics. We were able to use a MATLAB program for controlling the potentiostat to systematically vary the following experimental parameters: voltage, time, sampling rate, gain, and experimental run number using our potentiostat control function. All of the experiments were monitored in real-time using MATLAB plots of voltage vs. time, current vs. time, and total charge vs. time.

A wide array of experiments were performed, and we used an Excel spreadsheet to record the parameters described above, the substrate patterning and membrane use. Our experimental runs included deposition onto a gold surface with and without the membrane and gold electrodes with and without a membrane. Initial experiments allowed us to verify the complete experimental setup and determine the appropriate values for experimental parameters. We performed a total of 32 experiments, each with a different set of experimental conditions.

We used a Dektak II profilometer and a field emission scanning electron microscope (FESEM) to verify nanorod thickness and appearance. The profilometer allowed us to measure the film thicknesses. The FESEM allowed us to obtain high magnification images of our nanorods. A single row of nanorods is shown in Figure 3; the top image has a wide view of the sample at 35,000X and the bottom image focuses on the nanorods at an increased magnification of 50,000X. These images verify that the nanorods have dimensions consistent with the pore geometry in the membranes. Since we had to break the substrate to obtain a sample small enough for the FESEM, the nanorods were damaged in the process.

Ultimately we were able to culture HL-1 cardiomyocytes on the gold nanorod arrays. HL-1 cells are an electrically active cardiac cell line derived from rats. A transmitted light image was taken of the cells on the gold electrodes as seen in Figure 4. We were able to demonstrate the growth and viability of the cells on the nanorod electrodes surface. In addition we verified excellent cell adhesion, normal morphology and standard proliferation rate. Further testing will be required for a comparative study of the adhesion characteristics.

### **Acknowledgments:**

This would not have been possible without the funding of National Science Foundation and National Nanotechnology Infrastructure Network. Melanie-Claire Mallison and Trevor Thornton were very helpful and did an awesome job. Dr. Jennifer Blain Christen, my Principal Investigator, was wonderful and her level of involvement enhanced my experience. My mentors David Welch and Steve Herman were dedicated to helping me with my research. I will never forget this experience because I learned a lot about research and graduate school from the perspective of professors and students. Thanks again!!!

### **References:**

- [1] Choi, E; "The Silicon Chip: A Versatile Micro-Scale Platform for Micro and Nano-Scale Systems"; John Hopkins University, Thesis, 1-177(2008).
- [2] Moon, J and Wei, A; "Uniform Gold Nanorod Arrays from Polyethylenimine-coated Alumina Templates"; J Phys Chem B, 109(49), 23336-23341 (2005).
- [3] Evan P, Hendren W, Atkinson R , Wurtz G, Dickson W, Zayats and Pollard R; "Growth and Properties of gold and nickel nanorods in thin film alumina"; Nanotechnology, 17(2006), 5746-5753 (2006).
- [4] Martin, C; "Nanomaterials: A Membrane-Based Synthetic Approach"; Science, 266, 1961-1965 (1994).
- [5] Lu, G and Zhao; "Nanoporous Materials: An Overview"; Science and Engineering, Chapter 1, 1-12 (2004).

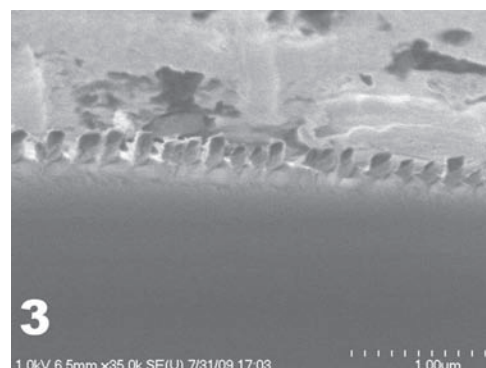


*Figure 3:  
FESEM images;  
single line of  
gold nanorods  
at 35,000X  
and 50,000X  
magnification.*

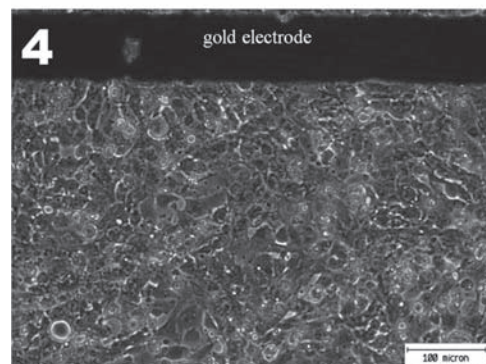
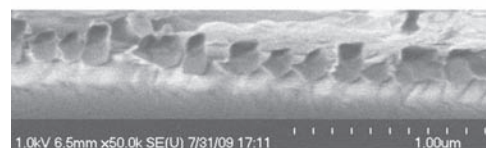


*Figure 4:  
Phase contrast  
image of  
cultured HL-1  
cardiomyocytes  
on Au nanorods.*

# Nanoporous Surfaces: Bioelectric Interfaces for Pathogen Detection

Lilian Gong

Biochemistry, Wellesley College

NNIN REU Site: ASU NanoFab, Arizona State University, Tempe, AZ

NNIN REU Principal Investigator(s): Shalini Prasad, Electrical, Computer, & Energy Engr, Arizona State University

NNIN REU Mentor(s): Gaurav Chatterjee, Srivatsa Aithal, ECEE, Arizona State University

Contact: lgong@wellesley.edu, shalini.prasad.1@asu.edu, gaurav.chatterjee@asu.edu, srivatsa.aithal@asu.edu

## Abstract:

The goal of this project was to build a biosensor to detect low concentrations of pathogens [1]. The purity of a liquid depends on the pathogens that contaminate it. We used a label free technique, which uses electrochemical impedance spectroscopy (EIS). By keeping our methods label free, detecting pathogens is cheaper and less time consuming, as compared to conventional methods. We used a printed circuit board (PCB) based-device and an alumina membrane to generate a nanoporous surface. By overlaying the membrane on top of the interdigitated electrodes of the PCB, a high-density array of nanowells was formed, which facilitated nano-confinement and allowed for size based trapping of the pathogens. We used layer-by-layer chemistry. The membrane was functionalized such that the cationic polymer attached to the membrane. The endotoxin, being anionic, bound to the cationic polymer, forming an electrical double layer. The variations in the impedance of the electrical double layer due to the changes in the concentrations of the pathogen were characterized using EIS. We have identified the performance parameters of the biosensor for pathogen detection.

## Introduction:

Testing the quality of drinking water for bacterial contamination is important because by testing for low concentrations of pathogens, many illnesses that are contracted via polluted water, such as cholera, can be avoided [2].

This summer we embarked on the first steps of building the said biosensor that would be portable, fast, and cost efficient. This was accomplished by using a label free technique, electrochemical impedance spectroscopy (EIS). In order to use EIS to characterize the impedance changes that occurred for different concentrations of endotoxins, layer-by-layer chemistry was used to modulate the charge in the electrical double layer at the solid/liquid interface, which allowed us to detect specific stepwise changes in impedance, that occur for the different dose concentrations of the endotoxin.

## Materials/Methods:

The materials used include an alumina membrane with a nanoporous surface, polyacrylic acid (PAA), a cationic polymer, and an endotoxin (Lipopolysaccharide, LPS). Having an alumina membrane with pores that have an upper diameter of 200 nm and a lower diameter is 20 nm was crucial because when the membrane is placed on top of the interdigitated electrodes, it forms a high-density array of nanowells, which facilitate nano-confinement of the cationic polymer and allow for size based trapping of the endotoxin. Size matching is important because it allows for an increase in the binding efficacy of the endotoxin, which amplifies the signal. Layer-by-layer chemistry [3], which was used to create an electrical double layer, was accomplished by

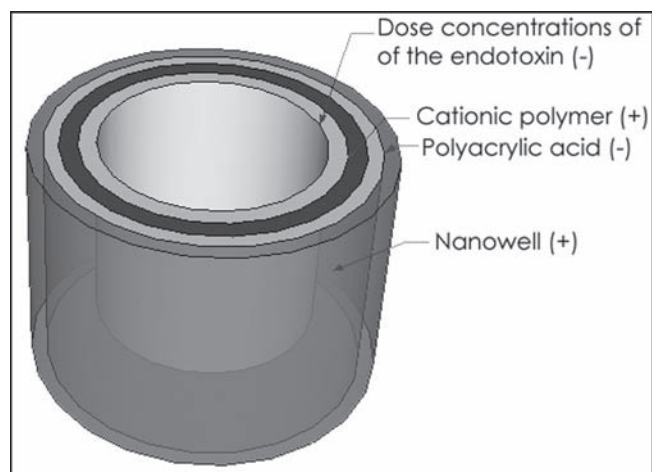


Figure 1: Layer-by-layer chemistry.

first functionalizing the nanoporous membrane with PAA. PAA was used as an adhesion layer between the alumina membrane and the cationic polymer. The endotoxin was the final layer added. This is illustrated in Figure 1.

When all the species bind together, they create an electrical double layer. The electrical double layer acts like capacitance. As the capacitance changes, so does the impedance of the system. Electrochemical impedance spectroscopy (EIS) [4] was used to characterize the system by measuring the change in impedance that occurred at different frequencies. This was accomplished by applying a voltage across a range of frequencies, measuring current, and calculating

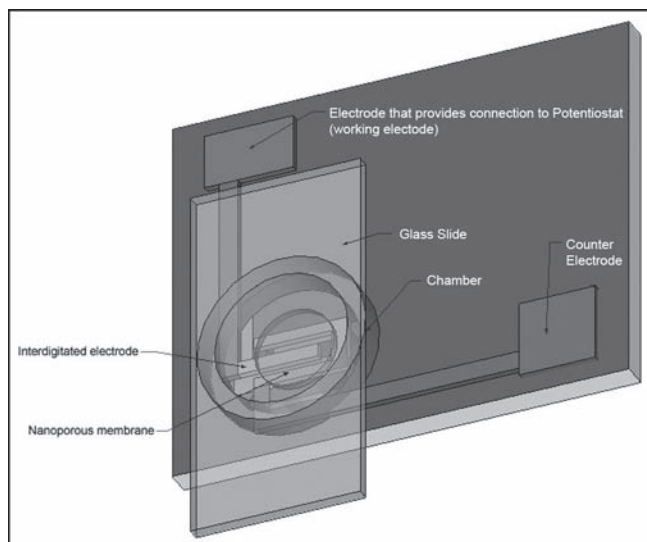


Figure 2: Experimental set-up.

the impedance at each frequency. This is called frequency response. When the frequency response is obtained for different doses, it is called the dose response. Figure 2 shows the experimental setup.

### Results:

There were two experiments conducted, one with PEI-25, and the other with NPGDE 1,5 BIS. PEI-25 is a commercially available polymer, which was used to establish the concept. NPGDE is a polymer that was synthesized specifically for our experiment.

**Experiment 1:** As seen in Figure 3 (dose response), the impedance normalized to a phosphate buffered saline (PBS) baseline was plotted across dose concentrations in micrograms per milliliter ( $\mu\text{g/ml}$ ). We took measurements for seven concentrations from 1-100  $\mu\text{g/ml}$ . Higher concentrations are not applicable for future applications as they are not clinically relevant.

**Experiment 2:** After the establishment of concept with PEI-25, NPGDE was used. Data was plotted in the same way as PEI-25, as shown in Figure 4. This time there were 11 LPS concentrations from 1-500  $\mu\text{g/ml}$ . Higher concentrations were tested for this run because less information is known about how this polymer interacts, and thus, performance parameters could be determined.

### Conclusion:

The device was shown to be capable of detecting endotoxins in the lower  $\mu\text{g/ml}$  regime. An increase in the measured impedance was observed for increasing concentrations of the endotoxin. There also appeared to be a significant increase in the impedance changes associated with endotoxin binding with the polymer NPGDE which indicated that NPGDE was more effective than PEI-25 at detecting endotoxins.

### Future Work:

Future plans involve screening a library of polymers to identify the polymer that will be the best match for endotoxin detection. Eventually this will lead to the development of a portable water quality monitoring device.

### Acknowledgements:

I would like to thank Shalini Prasad, Gaurav Chatterjee, Srivatsa Aithal, Trevor Thornton, Center for Solid State Electronics Research, and Rege lab at Department of Chemical Engineering, at Arizona State University. And the National Nanotechnology Infrastructure Network Research Experience for Undergraduates and National Science Foundation for funding.

### References:

- [1] Ivnitcki, D, Abdel-Hamid, I, Atanasov, P, and Wilkins, E (1998). Biosensors for detection of pathogenic bacteria. *Biosensors and Bioelectronics*, 14, 599-624.
- [2] Oram, Brian; Water Testing Bacteria, Coliform, Nuisance Bacteria, Viruses, and Pathogens in Drinking Water. Retrieved August 6, 2009, from Wilkes University Center for Environmental Quality Environmental Engineering and Earth Sciences Web site: <http://www.water-research.net/bacteria.htm>.
- [3] Bothara, M, Venkatraman, V, Reddy, R, Barrett, T, Carruthers, J, and Prasad, S (2008). Nanomonitors: electrical immunoassays for protein biomarker profiling. *Nanomedicine*, 4, 423-436.
- [4] D. Shinn-Jyh, Chang, B-W, Wu, C-C, Chen, C-J, and Chang, H-C (2007). A new method for detection of endotoxin on polymyxin B-immobilized gold electrodes. *ScienceDirect*, 9, 1206-1211.

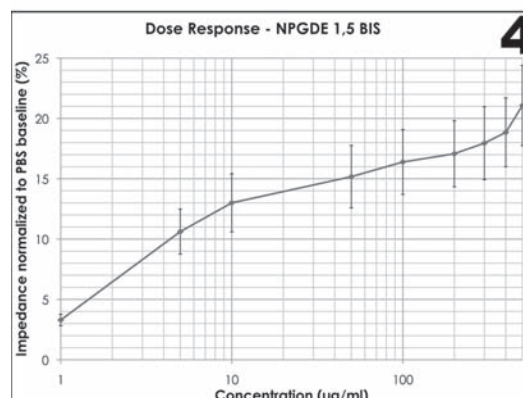
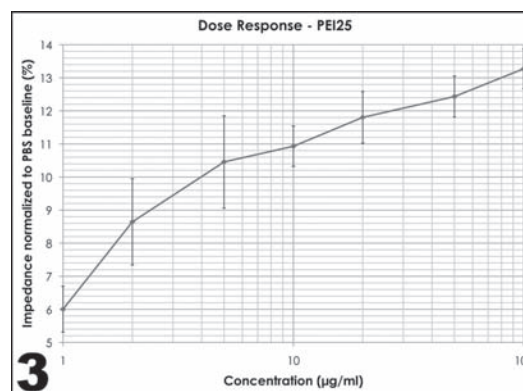


Figure 3: Dose response of PEI-25.

Figure 4: Dose response of NPGDE 1,5 BIS.

# Nanostructured Scaffolds for Tissue Engineering Applications

Nathaniel Hoglebe

Chemical Engineering, University of Dayton

**NNIN REU Site: Nano Research Facility, Washington University in St. Louis, St. Louis, MO**

**NNIN REU Principal Investigator(s): Dr. Younan Xia, Biomedical Engineering, Washington University in St. Louis**

**NNIN REU Mentor(s): Dr. Jingwei Xie, Biomedical Engineering, Washington University in St. Louis**

**Contact: hogrebj@notes.udayton.edu, xia@biomed.wustl.edu, xiej@seas.wustl.edu**

## Abstract:

Polymeric nanofiber scaffolds with both random and aligned fiber orientations were fabricated through the process of electrospinning. A linear gradient of the bone mineral hydroxyapatite was successfully deposited onto the surface, and the bone mesenchymal stem cells of rats were then cultured onto the scaffolds. Preliminary results illustrate that a higher cell density was found on areas of low mineral content.

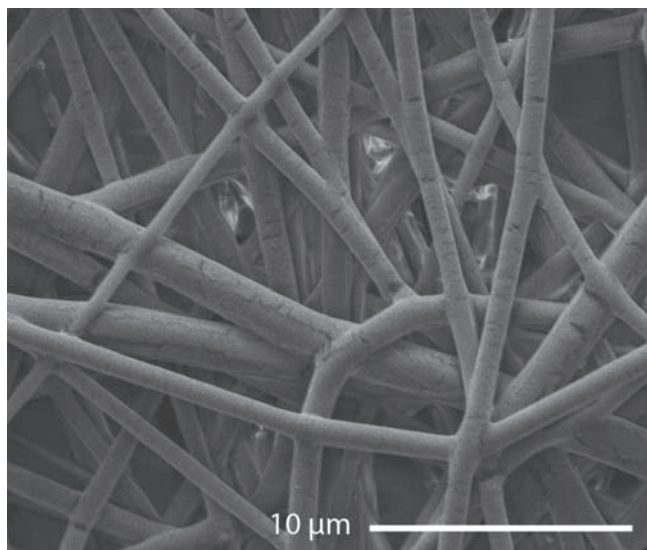


Figure 1: Scanning electron microscope (SEM) image of an unmineralized scaffold with random nanofiber orientation.

## Introduction:

One of the current challenges to successful implementation of tissue regeneration techniques into mainstream modern medical practice is the lack of the essential extracellular structure that promotes proper cell attachment, migration, proliferation, and differentiation. Nanofibers fabricated through the process of electrospinning the synthetic biodegradable polymer poly(lactic-co-glycolic acid) (PLGA) offer a promising prospect for this necessary scaffold in repairing damaged tissue because of their high porosity and large surface area [1].

In particular, when coated with a gradient of the bone mineral hydroxyapatite, these nanofibers can potentially mimic the tendon-to-bone attachment site, which is a place of much localized stress due to its non-uniform tissue composition as it changes from soft tendon to hard bone. The objectives of this project, therefore, were to fabricate PLGA nanofiber scaffolds with both random and aligned orientations of the

fibers, deposit hydroxyapatite onto the surface of the scaffolds in a gradient-like fashion, culture bone mesenchymal stem cells of rats onto these scaffolds, and finally characterize the cell activity in response to both varying concentrations of hydroxyapatite and orientations of the nanofibers in an effort to determine if these biomineralized scaffolds will be useful in the regeneration of damaged tendon-to-bone attachment sites.

## Experimental Procedure:

Electrospinning, the process by which a solution of dissolved polymer is turned into nanofibers, was used to fabricate the scaffolds. An electric current was applied to the tip of a syringe in order to induce a charge on the outgoing droplet, creating an electric field that stretched the dissolved PLGA into thin nanofibers as the solvent evaporated. The fibers were deposited on a uniform piece of aluminum foil to obtain a random orientation but were collected in the empty space between two pieces of metal to achieve a parallel formation of the nanofibers.

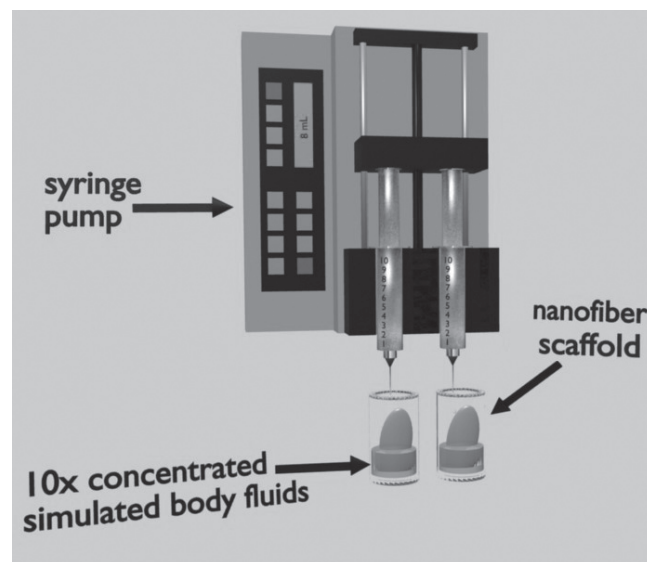


Figure 2: Schematic of the biomineralization process.

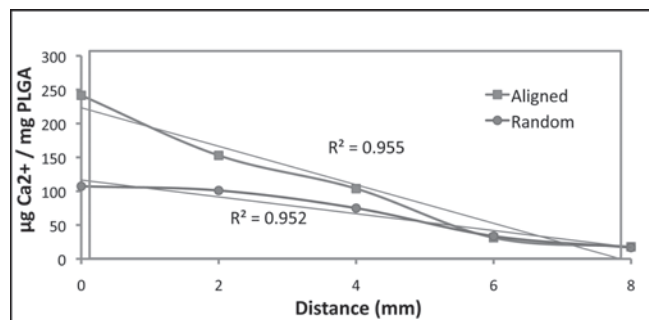


Figure 3: Graph of the mineral gradient.

Once the nanofibers were fabricated, the scaffolds were mounted onto copper wire frames and placed into glass vials. A gradient of hydroxyapatite was created by dripping 8 mL of a solution of ten times concentrated simulated body fluids and sodium bicarbonate over the course of an hour into the vials via a syringe pump. Since deposition is directly related to immersion time, the bottom of the scaffold obtained a higher concentration of mineral than the top, resulting in a linear gradient.

Once dried, the nanofiber scaffolds were mounted onto glass slides and prepared for cell culture. The bone mesenchymal stem cells (BMSC) of rats were grown onto the scaffolds using standard cell culture techniques using both proliferating and differentiating media. The scaffolds were monitored throughout the growth period for their attachment, proliferation, and differentiation characteristics in response to varying mineral content and nanofiber orientation.

### Results and Conclusions:

The calcium ion concentration was measured with both inductively coupled plasma mass spectroscopy (ICP-MS) and energy dispersive x-ray spectroscopy (EDX) to determine hydroxyapatite content. The results indicate a relatively linear deposition pattern corresponding to immersion time. After seven days of cell culture on the scaffolds with gradations in mineral content, preliminary results suggest that cell proliferation was greater in areas of lower mineral content.

This outcome can possibly be attributed to the fact that the scaffolds retain a higher porosity in regions of lower mineral content, and thus there are more sites to which the cells can attach. This result was surprising, however, because of its apparent contradiction with previous work, but it could be due to variations in the cell culture process, such as the use of different cell types [2]. Rat bone mesenchymal stem cells, for example, could possibly retain a fibroblast phenotype and thus tend to attach on a site with lower mineral content.

Alkaline phosphatase staining was used to determine the differentiation characteristics of the bone mesenchymal stem cells in differentiating media. Fluorescence micrographs indicate that there was a higher concentration of osteoblasts in areas of low mineral content, which can be attributed to the fact that there was an overall higher cell concentration in these regions.

The result of immunohistochemistry tests indicate that bone mesenchymal stem cells secreted type I collagen on both the high and low mineral content regions, while they secreted very little type II collagen anywhere on the scaffolds. This outcome indicates the development of cells with characteristics of tendon and bone cells. If type II collagen secretion was desired to mimic the fibrocartilage found between tendon and bone, alterations in the cell culture process could be performed.

### Future Work:

The preliminary results indicate that nanofiber scaffolds coated with a non-uniform layer of hydroxyapatite hold much promise for the regeneration of the tendon-to-bone interface due to their ability to yield a gradient of cell proliferation and behavior, which is critical to the structural integrity of the attachment site. Further research includes current in vivo experimentation of rat rotator cuffs that will attempt to determine the full extent of nanofiber scaffold utility in modern regenerative medicine.

### Acknowledgments:

This research was made possible through the National Science Foundation and the National Nanotechnology Infrastructure Network Research Experience for Undergraduates Program. I would also like to thank Amy Sears and everyone at the Nano Research Facility at Washington University in St. Louis, my mentor Jingwei Xie, and Principal Investigator Younan Xia.

### References:

- [1] Xie, J., X. Li, X. Xia. Putting electrospun nanofibers to work for biomedical research. *Macromolecular Rapid Communications* 2008; 29:1775-1792.
- [2] Li, X., et al. Nanofiber scaffolds with gradations in mineral content for mimicking the tendon-to-bone insertion site. *Nano Letters* 2009; 9:2763-2768.

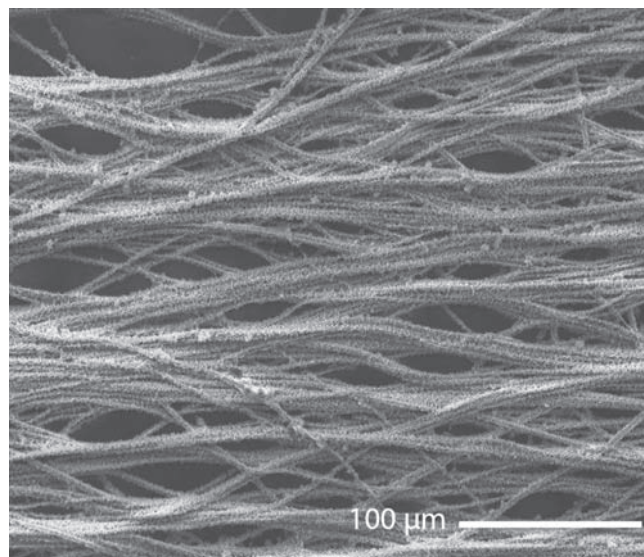


Figure 4: SEM of aligned nanofibers coated with mineral.

# Antimicrobial Effects of Metal Oxide Nanoparticles

Angela K. Horst

Biochemistry, Clarke College

NNIN REU Site: Nano Research Facility, Washington University in St. Louis, St. Louis, MO

NNIN REU Principal Investigator(s): Dr. Yinjie Tang, Department of Environmental and Chemical Engineering, Washington University in Saint Louis

NNIN REU Mentor(s): Dr. Bing Wu, Environmental and Chemical Engr., Washington University in Saint Louis

Contact: [angela.horst@clarke.edu](mailto:angela.horst@clarke.edu), [yinjie.tang@seas.wustl.edu](mailto:yinjie.tang@seas.wustl.edu)

## Abstract and Introduction:

In a world of emerging nanotechnology, one of the primary concerns is the potential environmental impact of nanoparticles (NPs). An efficient way to estimate nanotoxicity is to monitor the response of bacteria exposed to these particles [1]. This experiment explored the antimicrobial properties of nickel oxide, cobalt (II,III) oxide, zinc oxide, copper (II) oxide, iron (III) oxide, titanium dioxide, and iron (II,III) oxide against a model microorganism, *Escherichia coli*. The toxicity of these metal oxide NPs was tested using two methods: culturing in liquid media containing NPs, and electrospraying the NPs directly onto bacterial surface.

Aqueous exposure mimics the natural interaction between microbial species as NPs diffuse in the environment [2]. During these tests, there was noticeable aggregation, preventing effective interaction between the particles and the bacteria. The limited growth inhibition observed from this form of exposure to metal oxide NPs was therefore attributed to their ionic species.

On the other hand, the electrospray technique allows direct interaction between the NPs and cells. This exposure method grants insight into how “nano” associated properties from metal NPs affect the environment [2]. This method observed a higher death rate when the bacteria were exposed to oxidized nickel, zinc, and cobalt species; but no antimicrobial properties from titanium or iron. The disparity in the results of the two exposure techniques indicates that toxicity is dependant both upon the exposure method and the size of the particle.

## Experimental Procedure:

*Escherichia coli* (*E. coli*) were cultivated in M9 minimal media at 37°C. Optical density was measured at 600 nm (OD<sub>600</sub>) using a UV spectrometer (Genesys, Thermo-Scientific, USA). Experiments began with a 5 mL *E. coli* culture with OD<sub>600</sub> = 0.05 in M9 minimal media. The aqueous exposure method tracked the growth rate of *E. coli* with 2,

NP	Aqueous	Electrospray	Ionic
CuO	NT	N/A	T>2µg
NiO	NT	T	T>2µg
Co3O4	NT	T	T>2µg
ZnO	NT	T	NT
Fe2O3	NT	NT	NT
Fe3O4	NT	NT	NT
TiO2	NT	NT	NT

Table 1: Summary of results. T= toxic, NT = non-toxic.

20, and 100 mg/L NPs. OD<sub>600</sub> was recorded at 3, 6, 9, 21, 24 hours. The experiment was also performed using equivalent amounts of soluble chloride salt of the metals to test ionic toxicity.

For electrospray exposure experiments, the aliquot of *E. coli* was first filtered onto a polyvinylidene fluoride (PVDF) membrane (0.22 µm pore size, 1.25 cm × 1.25 cm, Millipore, US) to form a biofilm, which was then electrosprayed with NPs. The electrospray system was kept at a flow rate of 5 µL/min and a current of ~ 7 kV to maintain a cone shaped spray; the particles were suspended in 1.0 M sodium phosphate (Na<sub>2</sub>HPO<sub>4</sub>, pH 7) buffer. Then the biofilm was washed from membrane using minimal medium and the total living cells after electrospray exposure was measured based on the colony forming unit (CFU) using LB agar plates. Colonies were counted after the plates were incubated in 37°C for ~ 24 hours. Meanwhile, the cells from biofilm will be resuspended in the M9 minimal media and the recovery of growth was monitored by OD<sub>600</sub>. Scanning electron microscopy (SEM) was used to observe changes in cell morphology after exposure to NPs.

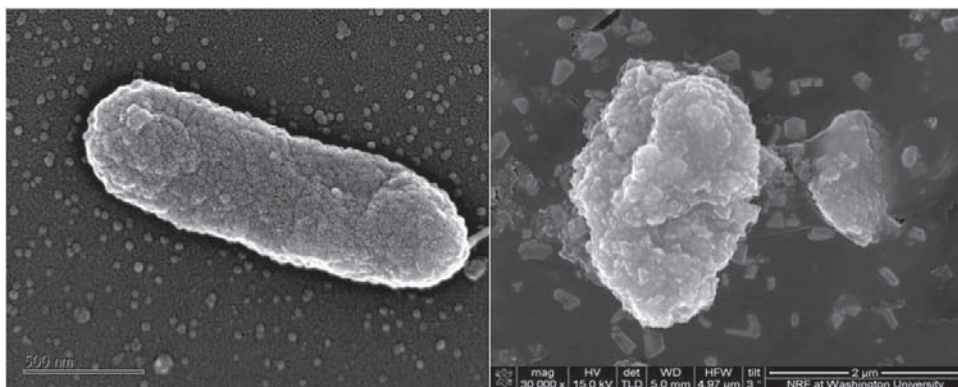


Figure 1: Comparison of an undamaged *E. coli* cell with one that has been electrospayed with nickel oxide.

electrical field, ionic zinc, and buffer were nontoxic. The next two bars show the inhibition when electrospayed with 4  $\mu\text{g/L}$  and 20  $\mu\text{g/L}$  zinc oxide NPs. This confirmed concentration has direct effect on toxicity. Next, the CFU after electrospaying with 4  $\mu\text{g/L}$  zinc oxide microparticles (480 nm diameter) confirms toxicity increases as particle size decreases. Finally, the CFU of *E. coli* exposed to titanium dioxide was used as a reference between zinc oxide and a nontoxic metal oxide.

### Results and Conclusions:

The growth curves from the aqueous exposure method displayed no growth inhibition from NPs, because all NPs aggregated. All ionic species, excluding iron and titanium, were inhibitory above 2  $\mu\text{g/L}$ . Growth curves show that the electrospay exposure method was able to cause significant cell death when *E. coli* was exposed directly to nickel oxide, cobalt (II, III) oxide, and zinc oxide (nickel oxide shows highest toxicity). The *E. coli* grew more efficiently and consistently when electrospayed with iron oxide NPs, were unaffected by titanium dioxide NPs, and copper (II) oxide was unclear. These results are summarized in Table 1. Figure 1 compares an undamaged *E. coli* cell with one that has been electrospayed with nickel oxide.

Zinc oxide exposure was tested more thoroughly than the other metal oxides and the inhibition from electrospay exposure was clearly observed as function of doses and sizes. Figure 2 shows the increase in recovery time after electrospaying (solid square), as opposed to recovery from aqueous exposure (diamond), and uninhibited growth (open square). The complete results from zinc oxide testing can be seen in Figure 3. From left to right, the non-sprayed bacteria show a similar CFU to those electrospayed with water, zinc chloride, and sodium phosphate buffer. This confirmed the

### Future Work:

The CFU data collected from some metal oxide NPs was too inconsistent for conclusions. We will repeat these experiments and collect CFU data after electrospaying. Tunneling electron microscopy (TEM) images have been suggested to identify whether NPs entered into cells after electrospaying.

### Acknowledgements:

Dr. Yinjie Tang and Dr. Bing Wu, for support, mentorship, and time. Dr. Yi-Shuan Lee for electrospaying. Washington University in St. Louis for use of their facilities, and National Nanotechnology Infrastructure Network Research Experience for Undergraduates Program and National Science Foundation for funding and making this all possible.

### References:

- Brayner, R. "The toxicological impact of nanoparticles." *Nanotoday* 3, 48-55 (2008).
- Wu, B. "New investigation of nano-ZnO antimicrobial activity." Submitted to *Environmental Science and Technology* (2009).

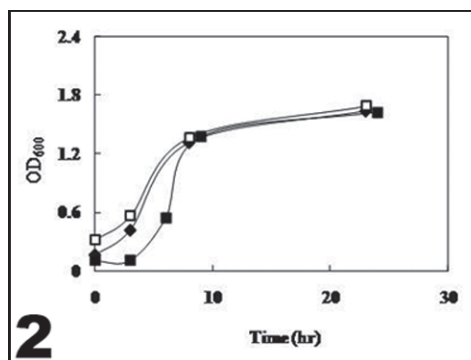


Figure 2: Increase in recovery time after electrospaying (solid square), as opposed to recovery from aqueous exposure (diamond), and uninhibited growth (open square).

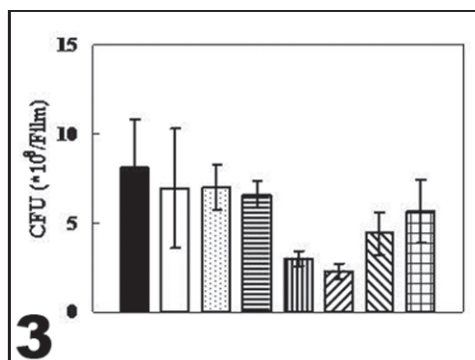


Figure 3: Complete results from zinc oxide testing.

# Optical Detection of Thrombus Formation within a Microfluidic Device using a Helium-Neon Laser as a Radiation Source

Adam Kozak

Biomedical Engineering, University of Rochester

NNIN REU Site: Nanotechnology Research Center, Georgia Institute of Technology, Atlanta, GA

NNIN REU Principal Investigator(s): Craig Forest, Assistant Professor of Mechanical Engineering, Georgia Tech

NNIN REU Mentor(s): Melissa Li, Biomedical Engineering, Georgia Institute of Technology

Contact: akozak2@u.rochester.edu, cforest@gatech.edu, melissa\_li@gatech.edu

## Abstract:

Understanding the dynamics of blood clotting, or thrombosis, is critically important to clinical evaluations of patients and to research laboratories studying diseases and drug effects. Particularly, the necessary conditions for late-stage acute thrombus formation are not well understood, and instrumentation has been limited in this context. The emerging field of microfluidics has led to significant advances in examining thrombus formation *in vitro*, allowing biologically relevant geometries and the measurement of volumetric growth rates in real time. However, current techniques (antibody binding, microscopic imaging) produce data with poor temporal and spatial resolution for accurate rate measurements. We present a method for detecting thrombus formation within a microfluidic device using a helium-neon laser, taking advantage of the low optical absorbance of platelets relative to erythrocytes. This method provides sub-second time resolution and a smaller instrument footprint compared to existing art. Our method is also capable of measuring the hematocrit of the blood being tested, as established in previous art [1], and which has been shown to affect thrombus growth in the past [2].

## Introduction:

The optical properties of blood have been well defined in existing literature. The most pertinent of these in our efforts is the transmissive properties of erythrocytes and platelets within the visible spectrum, since these are the primary constituents of thrombi. In the red portion of the spectrum, erythrocytes exhibit minimal transmittance, while platelets exhibit significant transmittance [3]. Under high blood shear conditions, which are analogous to those present within mammalian hearts, thrombus forms primarily composed of platelets. Thus as the thrombus grows, its transmittance increases measurably in relation to the surrounding blood.

## Construction:

Our research group had previously designed and manufactured a low-volume, high-throughput microfluidic device with several stenoses that exhibited shear rates between  $4000\text{s}^{-1}$  and  $7500\text{s}^{-1}$  (modeled through Poiseuille Flow and Particle Image Velocimetry). Porcine blood of known hematocrit (determined through centrifugation) was delivered via gravity pump into the microfluidic device which was placed upon an x-y stage for positioning.

Light from a 0.7 mW 632.8 nm helium-neon laser was passed through a series of mirrors and illuminated a single stenosis as shown in Figure 1. The transmitted light was measured by a photodiode and accompanying circuit, which provided a variable gain between  $3\text{E}+5$  and  $1\text{E}+7$ . The output was

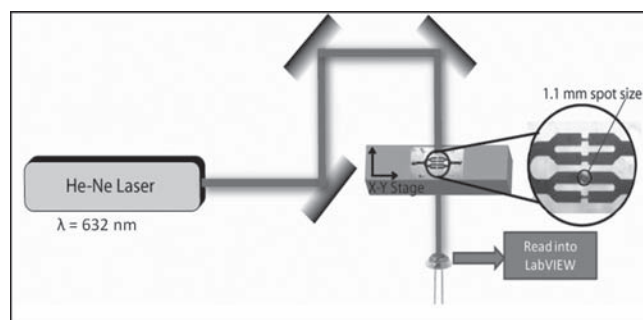


Figure 1: Schematic of the instrumentation for the single channel thrombosis measurement.

read by a National Instruments Data Acquisition Device into LabVIEW where a butterworth bandpass filter was applied and a moving average was taken.

However, the aforementioned construction was only able to measure a transmittance function within a single channel. Desiring to measure thrombus formation within multiple stenoses simultaneously, our construction was modified accordingly. To accomplish this, the incident light was diverged in one dimension utilizing a BK7 uncoated cylindrical lens. This light was then passed through an acrylic aperture plate placed on top of the microfluidic device, which contained four  $1000\ \mu\text{m}$  apertures separated to match the channel spacing. The transmitted light was

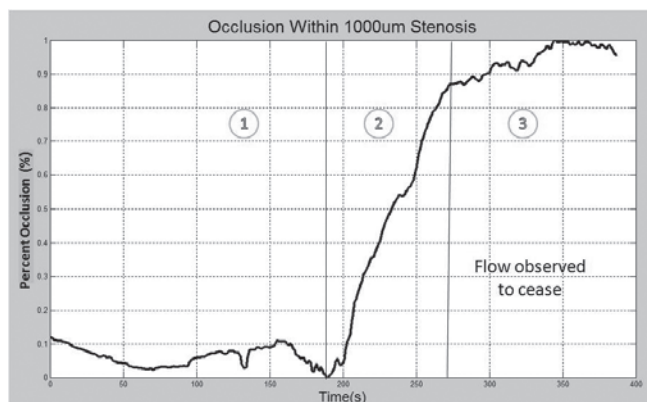


Figure 2: Photodiode output with three stage of thrombus formation labeled.

measured by a line CCD camera and read into LabVIEW for post-processing, as shown in Figure 2.

**Results:**

Thrombus growth was successfully measured in individual channels of the microfluidic device and was verified by comparison with microscopic imaging methods using identical blood samples and measuring at equivalent shear rates, as shown in Figure 3. Our method was able to measure the three distinct phases of thrombus formation: adhesion, acute growth, and occlusion, as shown in Figure 4. Volumetric thrombus growth could be measured with a sampling rate of up to 10 kHz, compared to microscopic imaging which operates at sub-hertz acquisition speeds.

Our method also provided a method of determining the hematocrit of the blood being measured. The initial intensity of the transmitted light is proportional to the concentration of erythrocytes, and thus can be related to the blood hematocrit with an error of approximately 2%.

Utilizing the high-throughput construction, growth has been observed in four stenoses simultaneously in addition to spatial localization of the growth within each stenosis.

**Discussion:**

Utilizing this method, differential thrombus formation has been observed under various blood parameters, such as

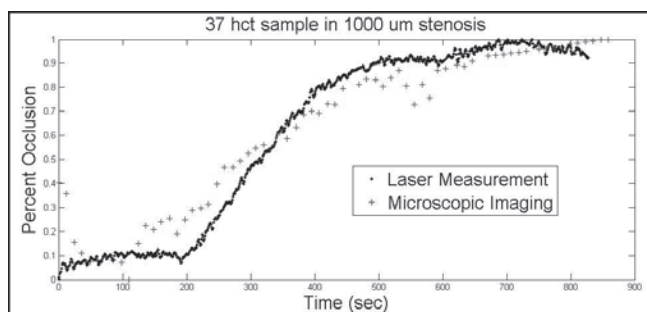


Figure 3: Comparison of laser detection with existing microscopic imaging (high frequency data corresponds to laser output).



Figure 4: Schematic of the instrumentation for multi-channel thrombosis measurement.

varying hematocrit, shear rate, and dosage of acetylsalicylic acid, an anti-thrombotic drug. However, more data is required before definitive analysis can be performed from a biological viewpoint.

The methods described above provide a superior method of detection over current art that can be expanded to perform large numbers of trials simultaneously. Additional tests are being conducted to validate the accuracy of the high-throughput instrumentation in comparison to the single-channel measurements. However, initial data indicates that it will be as accurate, in addition to providing previously unavailable spatial resolution.

**Conclusion:**

Described is a method of quantitatively analyzing acute volumetric thrombus growth. The method described provides not only a high time resolution, but also a smaller laboratory footprint and data load than existing art. The presented method is multifunctional, allowing an assessment of acute thrombus growth rate, time to occlusion, and the hematocrit of the blood being analyzed. Additional functionality can be added such as measuring hemoglobin concentration by observing the blood's optical scattering. Utilizing the presented method, the effects of drugs such as acetylsalicylic acid can be examined under different conditions, such as varied shear rates that simulate individuals with various stages of heart disease.

**Acknowledgements:**

The National Science Foundation, National Nanotechnology Infrastructure Network Research Experience for Undergraduates (NNIN REU) Program, and Georgia Institute of Technology.

**References:**

- [1] Cullis, H.M., Method and Apparatus for Making a Rapid Measurement of the Hematocrit of Blood, U.S. Patent 4 303 336, 1981.
- [2] Ross, J. M., L. V. Mcintire, et al. (1995). "Platelet-Adhesion and Aggregation on Human Type-VI Collagen Surfaces under Physiological Flow Conditions." *Blood* 85(7): 1826-1835.
- [3] Optical Properties of Circulating Human Blood in the Wavelength Range 400-2500 nm; Andre Roggan, Moritz Friebel, Klaus Dorschel, Andreas Hahn, and Gerhard Muller, *J. Biomed. Opt.* 4, 36 (1999), DOI:10.1117/1.429919.

# Modeling Intermediates in Prion Protein Fibril Formation

Sin Ying Stephanie Lau  
 Chemistry, Wellesley College

**NNIN REU Site:** Center for Nanotechnology, University of Washington, Seattle, WA  
 NNIN REU Principal Investigator(s): Prof. Valerie Daggett, Bioengineering, University of Washington  
 NNIN REU Mentor(s): Dr. Marc van der Kamp, Bioengineering, University of Washington  
 Contact: slau@wellesley.edu, daggett@u.washington.edu, mwvdk@u.washington.edu

**Abstract:**

The misfolding and aggregation of the prion protein have been implicated in several fatal neurodegenerative diseases. Misfolded prion proteins first aggregate into toxic, infectious protofibrils before forming fibrils. We constructed different protofibril models from molecular dynamics simulations of the human prion protein under misfolding conditions. These protofibril models were compared with experimental data to assess if they are reasonable models for the toxic intermediates.

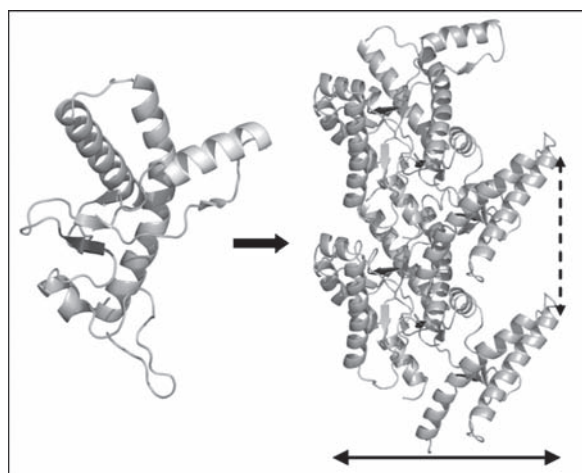


Figure 1: Left: Misfolded human PrP at pH 5. Right: Side view of a protofibril model. The dotted line indicates the rise per turn, while the solid line indicates the diameter of the model.

**Introduction:**

Aggregates of an abnormal form of the prion protein (PrP) are responsible for a group of fatal neurodegenerative conditions known as prion diseases, which include bovine spongiform encephalopathy (mad cow disease) and Creutzfeldt-Jakob disease. Prion diseases are caused by the misfolding and aggregation of PrP, which may be triggered by low pH or mutations. The structures of misfolded PrP cannot be determined experimentally, so our group used molecular dynamics to simulate the misfolding of PrP at various pH levels and with different mutations.

Misfolded prion proteins first assemble into soluble protofibrils before forming insoluble fibrils (Figure 1). There is evidence that protofibrils are toxic and infectious, and knowing the structure of these protofibrils can help us understand and combat prion diseases. Currently there is no high-resolution experimental data on protofibril structure,

but experiments have shown that misfolded PrP aggregates have significantly more  $\beta$ -structure and less  $\alpha$ -helical content compared with the natively-folded PrP. Experiments also indicated that residues 98-110 and 136-140 are important for aggregation and are likely on the binding interface between monomers [1].

Building on previous work [2], this project aimed to construct alternative human protofibril models with increased  $\beta$ -sheet content. We have built several models that are consistent with many available experimental data. (See Figure 1)

**Methods.** Misfolded conformations were selected from molecular dynamics simulations of PrP under misfolding conditions and docked manually to create models with cross-monomer  $\beta$ -sheets [2]. All models were constructed using PyMOL [3].

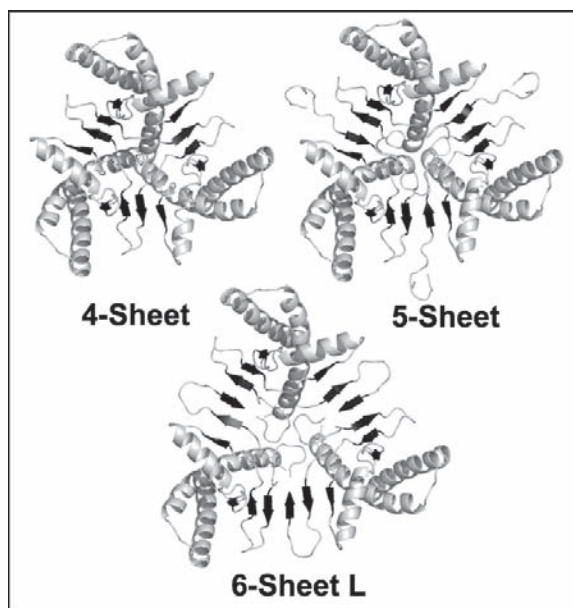


Figure 2: Top views of the left-handed spiral models.

**Prion Protofibril Models.** The human protofibril models we constructed are named according to the number of strands in the cross-monomer  $\beta$ -sheets. 4-sheet, 5-sheet, and 6-sheet L are left-handed spiral models built from misfolded wild-type PrP at pH 5 (Figure 2). All models have a repeating unit of three monomers. 4-sheet is similar to the previous protofibril models because each  $\beta$ -sheet has four strands. We were interested in building models with more  $\beta$ -structure, so we modeled one and two extra strands in the N-terminus to get 5-sheet and 6-sheet L, respectively.

While 6-sheet L has more  $\beta$ -structure, it also has more gaps in between monomers, which may make the model unstable. To make the model more compact while maintaining  $\beta$ -structure, we adjusted the 6-sheet conformations and fitted them into a right-handed spiral model, 6-sheet R, which has fewer gaps than its left-handed counterpart.

5-sheet D178N, whose cross-monomer  $\beta$ -sheet consists of five strands, was built from misfolded PrP conformations with the disease-causing mutation D178N. The mutated conformations only fit into a right-handed spiral, whereas the wild-type conformations fit readily into left-handed spirals.

To compare the different models, we measured the diameter and the rise per turn (Figure 1). The diameter increased with the increasing number of  $\beta$ -strands, but the rise per turn does not show a clear trend (Figure 3).

	4-Sheet	5-Sheet D178N	5-Sheet	6-Sheet R	6-Sheet L
# $\beta$ -strands	4	5	5	6	6
Handedness	Left	Right	Left	Right	Left
Diameter (Å)	67.1	72.7	74.3	79.4	81.1
Rise (Å)	37.5	37.5	40.5	34.5	40.5

Figure 3: Comparison of protofibril models.

### Comparison with Experimental Data:

To check if known antibody binding sites are accessible in our models, mapped epitopes were projected onto them (Figure 4). All models are accessible to the ICSM18 and H3:2 antibodies and, after some adjustments, also to R1. These three antibodies can bind to both native PrP and misfolded aggregates.

I5B3 and H3:3 bind selectively to misfolded PrP aggregates, and most of our models are accessible to them. Since I5B3 binds to three separate regions at once, the three regions must neighbor one another. This is indeed the case in our models (Figure 4). Furthermore, H3:3 binds to a region that is significantly altered during the misfolding simulations of PrP. The differences in the H3:3 binding region in native and misfolded PrP may explain the selectivity of H3:3 for PrP aggregates.

Finally, all our models can accommodate glycans at the known glycosylation sites, Asn-181 and Asn-197, and all have exposed proteinase K digestion sites at Gly-127.

### Conclusions and Future Work:

Structures representing misfolded PrP can be fitted into continuous spiral models with 4, 5, or 6  $\beta$ -strands. Two spiral conformations, left-handed or right-handed, are possible with 6  $\beta$ -strands. However, the models with 6  $\beta$ -strands show significant gaps, which may mean that these structures are unstable. Misfolded PrP with disease-related mutation D178N resulted in a different spiral model than wild-type misfolded PrP. Most of our models agree with available experimental data, indicating that the models are reasonable. More experimental data is needed to further assess if our models are representative of prion protofibrils.

### Acknowledgements:

I thank my PI Prof. Valerie Daggett, mentor Dr. Marc van der Kamp, and site coordinator Dr. Ethan Allen, for their assistance. I also thank the National Nanotechnology Infrastructure Network Research Experience for Undergraduates (NNIN REU) Program and National Science Foundation for funding.

### References:

- [1] Abalos G.C., Cruite J.T., Bellon A., Hemmers S., Akagi J., Mastrianni J.A., Williamson R.A., Solfrosi L. (2008) Identifying key components of the PrP<sup>C</sup>-PrP<sup>Sc</sup> replicative interface, *J. Biol. Chem.* 283, 34021-34028.
- [2] DeMarco M.L. and Daggett V. (2004) From Conversion to Aggregation: Protofibril Formation of the Prion Protein, *Proc. Natl. Acad. Sci.* 101, 2293-2298; Scouras A.D. and Daggett V. (2008) Species variation in PrP<sup>Sc</sup> protofibril models, *J. Mater. Sci.* 43, 3625-3637.
- [3] DeLano, W.L. (2002) The PyMOL Molecular Graphics System (Palo Alto, CA, USA, DeLano Scientific).

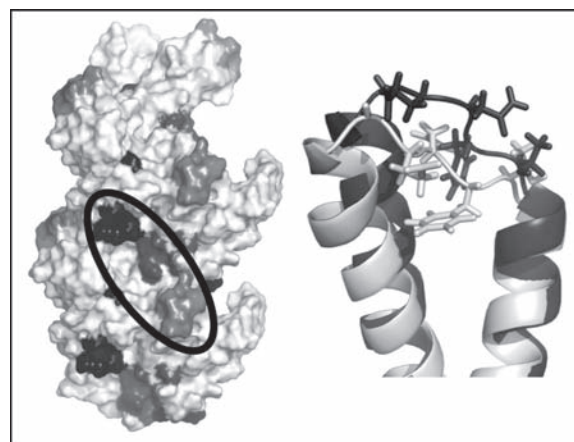


Figure 4: Left: I5B3 binding regions in the 4-sheet model. Right: Changes in the H3:3 binding region in native PrP (light gray) and misfolded PrP (dark gray).

# Characterization of Gold Nanoparticles Functionalized with Thiolated Single-Stranded DNA

Alexandra J. Machen

Chemical Engineering, University of Kansas

**NNIN REU Site: Center for Nanotechnology, University of Washington, Seattle, WA**

*NNIN REU Principal Investigator(s): Sirnegada Techane, Chemical Engineering, University of Washington*

*NNIN REU Mentor(s): Lara J. Gamble, Ph.D., David G. Castner, Ph.D., Bioengineering and Chemical Engineering, University of Washington*

*Contact: jaymac@ku.edu, castner@nb.engr.washington.edu, gamble@nb.engr.washington.edu, sdt5@u.washington.edu*

## Introduction:

Gold surfaces functionalized with deoxyribonucleic acid (DNA) are used in biomedical applications such as biosensing. When biosensors and other biomedical devices are placed in a biological environment, various reactions (analyte sensing, protein adsorption, etc.) will occur at their surface. For nanoparticles, where the surface-to-volume ratio is high, these surface properties are crucial and often unique from their larger scale counterparts [1].

Our work included functionalizing and characterizing gold nanoparticles (AuNPs) with thiolated single-stranded DNA (SH-ssDNA) in various buffers with different salt concentrations. We performed detailed surface analysis of the functionalized AuNPs using x-ray photoelectron spectroscopy (XPS). The SH-ssDNA functionalized AuNPs were then backfilled for varying amounts of time with hydroxyl-terminated alkylthiols to hinder DNA base-gold binding. Control flat Au surfaces were also functionalized with SH-ssDNA for comparison to the functionalized AuNPs.

## Experimental Methods:

**Materials.** The 40-mer SH-ssDNA [5'(C5-Thiol) AGC TGC CCT GGT AGG TT TCT GGG AAG GGA CAG ATG ACA G 3'] was purchased from Trilink Biotechnologies (lot U17-0209-AC1A-A). Ultrapure water (resistivity >18.0 M  $\Omega$  cm) used for preparing all aqueous solutions was purified by a Modulab Analytical research grade water system. Spectra/Por molecular porous membrane dialysis tubing was purchased from Sigma-Aldrich. Tubing-type 1 had a molecular weight cut off of 12-14,000 and tubing-type 2 had a molecular weight cut off 50,000 (wet in 0.1% sodium azide). All other chemicals were also purchased from Sigma-Aldrich.

**Gold Nanoparticle Stability.** UV/VIS measurements were performed to determine which buffer and salt conditions provided a stable environment for the AuNPs. A stable environment was considered one that did not cause the AuNPs to aggregate as identified by a change in color.

**Thiol-DNA Assembly.** Water, buffer, and SH-ssDNA were combined at the desired concentrations in a glass scintillation

vial and mixed for 30 seconds. AuNPs were added, and when relevant, solution was mixed for 30 minutes before adding salt. The AuNPs were functionalized for 24 hrs before purification. Samples were dialyzed 2x in tubing-type 1 and 10x in tubing-type 2 (see materials) in 3500 mL water.

**Backfilling Procedure.** 97.55  $\mu$ L of 9.0M hydroxyl-terminated alkythiol were added to 4 ml purified functionalized AuNPs. Samples were backfilled for varying amounts of time before being dialyzed 10x in tubing-type 2.

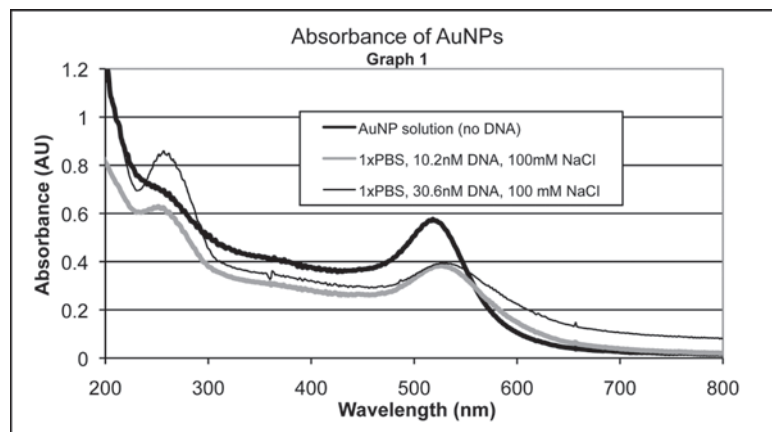
**XPS Analysis.** XPS measurements were performed on Surface Science Instrument S-Probe spectrometer with a monochromated Al-K $\alpha$  x-ray source. Compositional survey, detailed scans (Au4f, C1s, O1s, P2p, S2p and N1s) and high resolution scans (C1s and N1s) were acquired. All measurements were taken at a 55° photoelectron takeoff angle. The computational data are averages of values from two samples, three spots per sample. Data analysis was performed on the Service Physics ESCA 2000 Graphics Viewer data reduction software.

## Results and Discussion:

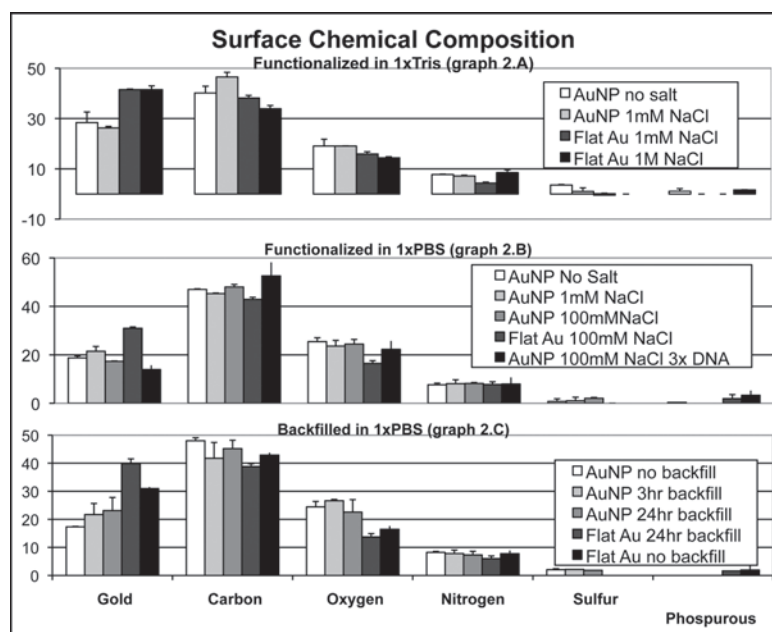
**Stability of AuNPs.** Adding SH-ssDNA to buffer before adding AuNPs helped decrease aggregation. Using this procedure, the highest stable salt concentrations in 1 $\times$  Tris and 1 $\times$  PBS were 1 mM NaCl and 100 mM NaCl, respectively. In both buffer systems, adding NaCl last allowed for a higher final salt concentration.

**UV/VIS Absorbance of AuNPs (Graph 1).** SH-ssDNA peaks appeared at 260 nm and gold peaks appeared around 525 nm. There was no SH-ssDNA peak in the AuNP solution before functionalization, as expected. The broadening of the gold peak in the functionalized samples indicated particle growth. This combined with the noticeable SH-ssDNA peaks suggested that SH-ssDNA had been attached to the AuNPs.

**Surface Chemical Composition of AuNPs (Graph 2).** Increasing the salt concentration of a sample was previously shown to increase the SH-ssDNA loading onto the surface by



Graph 1



Graph 2

shielding the DNA-DNA repulsion forces [2]. However, SH-ssDNA loading on the AuNPs was not significantly affected by the salt concentration. An increase in loading would result in a lower percentage of gold seen on the surface [3]. This was not the case in Tris buffer (Graph 2.A) or PBS (Graph 2.B).

It is possible the SH-ssDNA concentration was too low to be affected by the repulsion forces. However, increasing the SH-ssDNA concentration by 3x (Graph 2.B) did not significantly change surface composition. In PBS, AuNPs exhibited similar nitrogen composition compared to flat surface. In Tris, there were similar phosphorus compositions. Some samples also had high amounts of sulfur. This was most likely due to minor contamination.

Graph 2.C shows the chemical surface composition of functionalized AuNPs backfilled with 6-mercapto-1-hexanol

for 0, 3, and 24 hrs. The time allowed to backfill had little effect on alkythiol coverage on AuNPs. That is, the 3 hrs time range was long enough for the backfilling to be equilibrated; therefore, shorter times (< 3 hrs) are recommended for future studies. The flat surface comparison is also shown on Graph 2.C. Both the AuNPs and flat gold exhibited an increase in percentage of gold on the surface as backfilling occurred. This seems counter intuitive, but the hydroxyl-terminated alkythiols being added were significantly shorter than the 40mer SH-ssDNA. Hence, the alkythiols attenuated the gold signal less than the SH-ssDNA [3].

### Conclusions:

To develop understanding of the structure-function relationship for biomedical devices and optimize their performance, their surface properties must be characterized. In this study, 14 nm diameter AuNPs were functionalized with SH-ssDNA in Tris and PBS buffer in varying salt concentrations. Using surface analysis techniques for characterization, we determined adding salt did not enhance SH-ssDNA assembly for the DNA concentration used in this study. Control flat gold surfaces were subjected to similar conditions. All AuNP samples had lower percentages of gold than the flat surface samples. The curved surface of AuNP may have enabled higher SH-ssDNA loading. Also, compared to flat surfaces, the XPS organic overlayer signals are enhanced relative the underlying gold signals for AuNPs [4].

Further characterization and optimization of the DNA coated AuNPs is currently underway.

### Acknowledgements:

This research was supported by National Nanotechnology Infrastructure Network (grant ECS-0335765) Research Experience for Undergraduates Program (grant EEC-0649215), NESAC/BIO (NIH grant EB-002027), and the National Science Foundation.

### References:

- [1] Grainger D.W.; Castner, D.G. *Adv. Mater.* 2008, 20, 867-877.
- [2] Hurst, S.J.; Lytton-Jean, A.K.R.; Mirkin, C.A. *Anal. Chem.* 2006, 78, 8313-8318.
- [3] Lee, C.; Gong, P.; Harbers, G.M.; Grainger D.W.; Castner, D.G.; Gamble, L.J. *Anal. Chem.* 2006, 78, 3316-3325.
- [4] Lee, C.; Harbers, G. M.; Grainger, D.W.; Gamble, L.J.; Castner, D.G. *J. Am. Chem. Soc.* 2007, 129, 9429-9438.

# Development and Fabrication of a Micro-Microbial Fuel Cell

Isaac Markus

Chemical Engineering, The Cooper Union for the Advancement of Science and Art

NNIN REU Site: Cornell NanoScale Science and Technology Facility, Cornell University, Ithaca, NY

NNIN REU Principal Investigator(s): Dr. Largus T. Angenent, Biological and Environmental Engineering, Cornell

NNIN REU Mentor(s): Arvind Venkataraman, Biological and Environmental Engineering, Cornell University

Contact: markus@cooper.edu, la249@cornell.edu, av299@cornell.edu



Figure 1: Mask for channels.

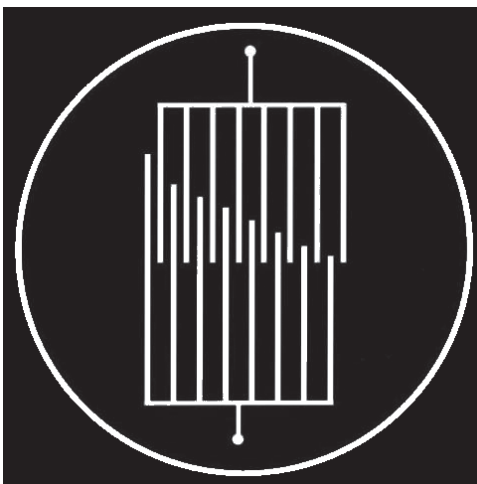


Figure 2: Mask for electrodes.

## Introduction:

Bioelectrochemical systems (BESs) have gathered attention in recent years because they convert organic material in wastewater into electricity and chemicals, and are applied as biosensors. Microbial fuel cells (MFCs) are one example of a BES in which anaerobic bacteria oxidize carbon sources using the anode as a terminal electron acceptor thereby generating a current. The bacteria grow planktonic as well as an anodic biofilm employing direct electron transfer and/or mediators for current generation. The biofilm density and composition are determining factors for the efficiency and power generation of MFCs. This project focuses on developing and fabricating a micro-microbial fuel cell ( $\mu$ MFC). We believe that by reducing the overall surface to volume ratio the Coulombic efficiency can be increased subsequently leading to higher power densities. Additionally, the  $\mu$ MFC can be used as a tool to study real time biofilm growth and development [1].

## Experimental Procedure:

**Mask Design.** The mask for the silicon (Si) masters and electrodes were design by Dr. Benjamin Steinhaus. The masks were printed through emulsion on transparent paper and the design is shown in Figures 1 and 2.

**Master Fabrication.** Masters were fabricated on 100 mm silicon wafers. The wafers were coated with P20 primer (2000 RPM at 1000 RPM/s) and then S1827 resist (2000 RPM at 500 RPM/s). Wafers were soft baked at 115°C for 90 sec, exposed for 16 sec placed in an ammonia image reversal oven, hard baked at 115°C for 90 sec and developed using MF321. Masters were etched using a Unaxis 770 Si etcher to a depth of 100  $\mu$ m. Remaining resist was removed using a resist hot strip bath. Wafers were finally coated with an

inert layer of 1H,1H,2H,2H-perfluorooctyl trichlorosilane (FOTS) using molecular vapor deposition.

**Electrode Fabrication.** Electrodes were fabricated on 100 mm borofloat wafers. Wafers were cleaned using isopropyl alcohol and acetone. The wafers were coated with P20 primer (2000 RPM at 1000 RPM/s) and then S1827 resist (2000 RPM at 500 RPM/s), soft baked at 115°C for 5 min, exposed for 16 sec, hard baked at 115°C for 5 min and developed using MF321. A titanium and gold layer (100/200 nm) was deposited using an SC4500 evaporator. Excess metal was removed by lifting off remaining resist using 1165 stripper.

**Microfluidic Device Fabrication.** The first device was cast with polydimethylsiloxane (PDMS), mixed in a 10:1 weight ratio with curing agent. The solution was degassed and poured over the Si master and cured for 2 hr at 90°C. PDMS was peeled away, and inlet and outlet holes were punched using 18G blunt needles. The second device was cast with a mixture of PDMS and zirconium n-butoxide. The latter chemical addition rendered the polymeric structure as a proton exchange membrane (PEM) [2]. Zirconium n-butoxide and ethyl acetoacetate were mixed in a molar ratio 1:1. This solution was then mixed with PDMS (95% PDMS by weight). The mixture was degassed and poured over the Si master. Solution was cured at 60°C for 2 hr and

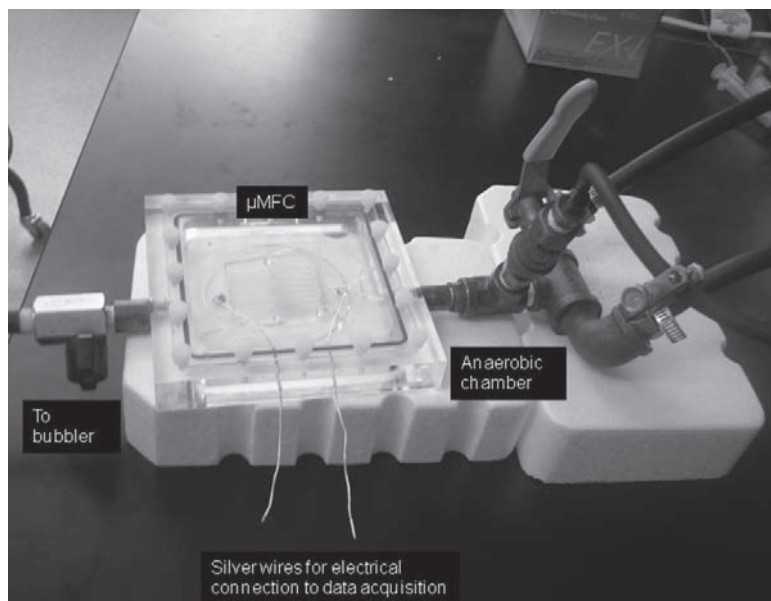


Figure 3: Experimental Setup.  $\mu$ MFC lies inside anaerobic chamber connected to syringe pump through tygon tubing. Electrodes are connected to data acquisition system with silver wires.

annealed at 120°C for two days. The PEM remained opaque, rendering it unsuitable for application.

**Experimental Setup.** The PDMS and the electrodes were exposed to plasma for 1 min and attached. Tygon tubing was connected to the inlets and outlets and sealed with epoxy. The electrodes were connected with silver wires to a Keithley voltmeter, which recorded the open circuit potential. The  $\mu$ MFC was operated under micro-aerobic conditions continuously for six days at a flow rate of 0.001 ml/min. The experiment setup is shown in Figure 3. A baseline was established by using 100 mM potassium ferricyanide in phosphate buffer as the catholyte and M4 media as the anolyte. The system was inoculated with 0.5 ml *Shewanella oneidensis* MR-I solution (grown overnight in Luria-Bertani) after 12 hours.

### Results and Discussion:

The open circuit voltage (OCV) prior to inoculation was 61 mV. Post-inoculation the potential increased to 255 mV after five days (Figure 4). The potential suggests that the  $\mu$ MFC still has a high internal resistance since theoretical values of 850 mV have been reported [3] for MFCs using the same catholyte and anolyte. This can be attributed to the device being made from PDMS, a low ionic conductor. The OCV was also reduced due to the device being operated under micro-aerobic conditions, since oxygen is a better electron acceptor than the anode.

### Conclusions and Future Work:

We successfully constructed a  $\mu$ MFC capable of operating at 255 mV. This initial prototype shows much promise and in the future can be improved by using a material with higher ionic conductivity such as a ZrO-PDMS mixture. Additionally, this potential can be increased by operating under anaerobic conditions, preventing the drain of electrons by oxygen.

### Acknowledgements:

This work was supported by National Science Foundation, National Nanotechnology Infrastructure Network Research Experience for Undergraduates (NNIN REU) Program and CNF. Additionally, it was possible thanks to Largus T. Angenent and Arvind Venkataraman.

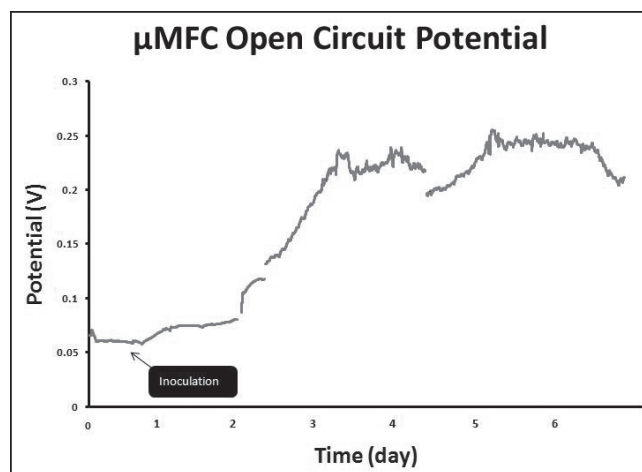


Figure 4: Open circuit potential results. The  $\mu$ MFC had a baseline OCV of 61 mV. The potential increased to 255 mV post-inoculation and stabilized at 235 mV.

### References:

- [1] Fornero J. J., Rosenbaum M., Cotta M. A. and Angenent L. T. "Microbial fuel cell performance with a pressurized cathode," *Environmental Science and Tech* Vol. 42, 22, 8578–8584 (2008).
- [2] Katayama, S. Kubo, Y. Yamada, N. "Characterization and Mechanical Properties of Flexible Dimethylsiloxane-Based Inorganic/Organic Hybrid Sheets," *Journal of the American Ceramic Society*, 85 [5] 1157-1163 (2002).
- [3] Rosenbaum, M. Zhao, F. Schroder, U. Scholz, F. "Interfacing Electrocatalysis and Biocatalysis with Tungsten Carbide: A High-Performance, Noble-Metal-Free Microbial Fuel Cell," *Angewandte Chemie*, 118, 1-4 (2006).
- [4] Du, Z. Li, H. Gu, T. "A state of the art review on microbial fuel cells: A promising technology for wastewater treatment and bioenergy," *Biotechnology Advances*, 25 [5] 464-482 (2007).

# Single Walled Carbon Nanotubes as Nanopores for DNA Translocation

Claire McLellan

Physics, Wake Forest University

NNIN REU Site: ASU NanoFab, Arizona State University, Tempe, AZ

NNIN REU Principal Investigator(s): Dr. Stuart Lindsay, Biodesign Institute, Arizona State University

NNIN REU Mentor(s): Dr. Jin He, Biodesign Institute, Arizona State University

Contact: mcleca8@wfu.edu, stuart.lindsay@asu.edu, jinhe@asu.edu

## Introduction:

Single molecule deoxyribonucleic acid (DNA) sequencing through nanopores is potentially a fast cost effective way to sequence long strands of DNA. Nanopores have a similar diameter to DNA, so DNA has to unravel itself when it is translocated through the nanopore, about 10 nm for double stranded DNA (dsDNA) and about 2 nm for single stranded DNA (ssDNA). The individual DNA bases can pass the nanopore in a sequential manner [1].

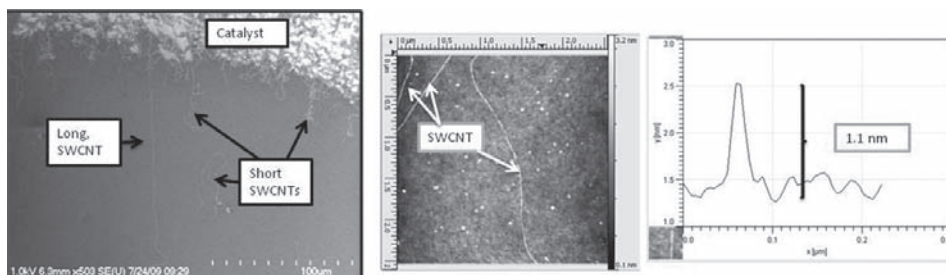


Figure 1: FESEM and AFM with height displacement graph for marker.

To translocate DNA, a voltage is applied across a nanopore that separates two reservoirs of aqueous electrolyte solution. The nanopore essentially becomes a Coulter counter. The ions in the electrolytes move through the nanopore and create an ionic current. DNA, which is a negatively charged molecule, is translocated through the pore by electrophoresis. DNA inside the SWCNT block the ion flow so a change in the ionic current is detected during translocation. Ionic current, as well as tunneling current and optical signal may be used as readout signals for nanopore DNA sequencing. Nanopore sequencing does not include all the complicated and time consuming processes of cloning, polymerase chain reaction, and capillary electrophoresis, potentially sequencing a diploid mammalian genome in 24 hours for about ~\$1000 [2].

Currently nanopores have been created that can discriminate dsDNA and ssDNA by the different pore sizes used for the translocation. Ribonucleic acid (RNA) and DNA are discriminated by differences in the amplitude of the ionic current and the translocation duration time. The length of the DNA is discriminated by a change in the time length when the ionic current is blocked [3].

Single walled carbon nanotubes (SWCNTs) are well structured, long, and natural nanopores with atomically flat inner walls. SWCNTs are about ~ 1-4 nm in diameter and can reach the millimeter scale in length although usually the micron scale. The channel form of the SWCNT provides a

way to contain DNA and potentially control the speed of the DNA when translocated past a base reader. In order to create a SWCNT translocation device, SWCNTs need to be well calibrated.

This summer we investigated SWCNT calibration by growing SWCNTs using a chemical vapor deposition (CVD) method and characterizing SWCNTs using atomic force microscopy (AFM) and field emission scanning electron microscopy (FESEM). We investigated the translocation capabilities of the SWCNTs by measuring the ionic current through the SWCNT based nanofluidic device.

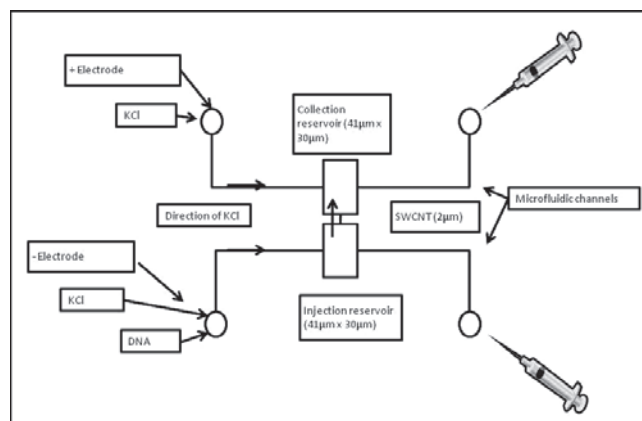


Figure 2: Schematic of DNA translocation device.

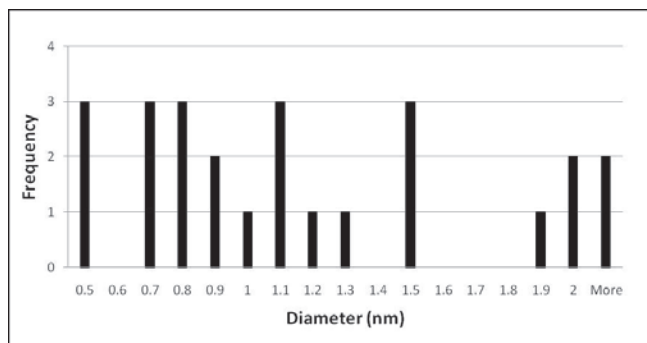


Figure 3: Histogram for SWCNT diameters.

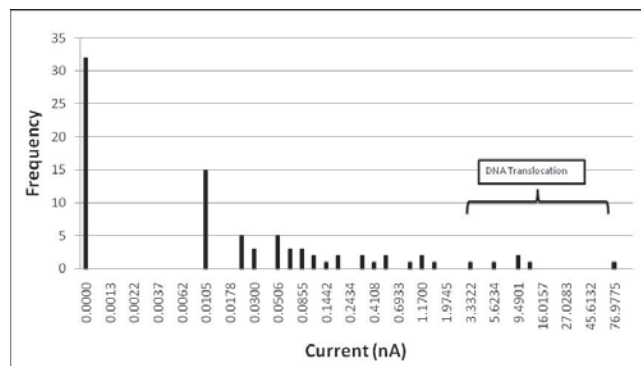


Figure 4: Histogram for SWCNT ionic currents.

**Methods and Materials:**

The CVD method gives control over SWCNT’s orientation, horizontal alignment, length, and diameter. CVD-grown SWCNTs have been shown to have less defects than other methods. The catalyst was produced by a mixture of diblock polymer and cobalt salt. Argon and hydrogen were the gas carriers for the carbon source, ethanol. Ethanol was chosen because the OH group effectively removes any amorphous carbon that would cover and deactivate the cobalt nanoparticles. AFM and FESEM images were used to characterize the grown SWCNTs (Figure 1). A polydimethylsiloxane (PDMS) microfluidic system was prepared and used to introduce solution to SWCNTs. Electron beam lithography (EBL) was used to create reservoirs in the PMMA resist layer that covered on top of the SWCNTs. Oxygen plasma was used to remove the exposed SWCNT in reservoirs and open both ends of the SWCNT that connected two reservoirs. The SWCNT was soaked with an aqueous potassium chloride (KCl) solution. A voltage was applied across the SWCNT for ionic current (Figure 2).

**Results and Discussion:**

The diameters of the SWCNTs found using AFM are illustrated in Figure 3. The spatial distribution was found using FESEM. The distribution distances were taken 100 μm from the catalyst on four silicon dioxide (SiO<sub>2</sub>) substrates. Usually surface density is used when studying distribution, but the SWCNTs were parallel so distances were found. The mean was 111 μm ± 98 μm. It was common to find many SWCNTs close to one another and then have hundreds of microns before another SWCNT was found. More SWCNT were found in the area closer to the catalyst. The CVD method of growing SWCNTs was successful in respect to growing many SWCNTs that were long and straight, well dispersed, with usable diameters. If a diameter was too small, the DNA could not translocate and if it was too large, the ionic current change was not obvious. The optimal diameter was 2 nm.

We tested the ionic current of the SWCNTs that had been etched by oxygen plasma and placed in a translocation device; the results are shown in Figure 4. Most, 67%, of the devices made were successful at transferring ionic current. Those devices that did not transfer current could have been contaminated, contained defects, or not opened entirely on each side. The SWCNTs that had successful ionic currents could be used for DNA translocation testing.

DNA translocation favors high ionic current. The distribution of currents may be caused by the distribution in diameter. It would be useful to study how to increase the yield of SWCNTs with high currents. Research in efficient DNA sequencing will help the understanding of the genome and its applications in medical research.

**Acknowledgements:**

I would like to acknowledge the National Science Foundation and the National Nanotechnology Infrastructure Network Research Experience for Undergraduates (NNIN REU) Program for providing the funding for this internship, Arizona State University for providing the facilities, Trevor Thornton for organizing the program, and Dr. Stuart Lindsay, Dr. Jin He and his graduate students for sharing their knowledge and laboratory.

**References:**

- [1] Austin, R. (2003). Nanopores: The art of sucking spaghetti. *Nature Materials*, 2, 567-568.
- [2] Branton, D., Deamer, D., Marziali, A., et al. (2008). The potential and challenges of nanopore sequencing. *Nature Biotechnology*, 26(10), 1146-1153.
- [3] Rhee, M. and Burns, M. A. (2006). Nanopore sequencing technology: nanopore preparations. *TRENDS in Biotechnology*, 25(4), 174-181.

# Nanomechanical Properties of Motor Proteins

Margaret Merritt

Biomedical Engineering, Brown University

**NNIN REU Site: Nanotech @ UCSB, University of California, Santa Barbara, CA**

*NNIN REU Principal Investigator(s): Megan T. Valentine, Mechanical Engineering, UCSB*

*NNIN REU Mentor(s): Dezhi Yu, Materials Science, University of California at Santa Barbara*

*Contact: Margaret\_Merritt@brown.edu, valentine@engineering.ucsb.edu, dezhi0622@umail.ucsb.edu*

## **Abstract:**

Motor proteins drive essential processes in the body, including muscle movement and cell division, by converting chemical energy to mechanical work. Yet, the relationship between the structure and function of these molecular motors is not well understood. Acquiring comprehensive knowledge of these interactions could ultimately lead to the creation of nanoscale proteins with tunable properties. Such proteins could vastly improve cancer and disease research as well as provide fundamental insight into cell biology. The present study aims to further investigate nanomechanical properties of kinesin, a motor protein responsible for intracellular transport. To accomplish this, we successfully generated a recombinant human kinesin construct, labeled with green fluorescent protein and a histidine epitope tag, and used high-resolution imaging to characterize its velocity and photostability *in vitro*.

## **Introduction:**

Kinesins are one group of motor proteins that transport cargo and play a critical role in cell division [1]. In cells, kinesin molecules attach to, “walk” along, and detach from microtubules, one type of cytoskeletal polymer, by a series of chemical reactions involving adenosine triphosphate (ATP) [2,3]. Kinesin proteins can be expressed in bacteria cells and characterized *in vitro*. Observing this walking process in reconstituted systems can help to better understand the relationship between kinesin and microtubules, and will provide insight into the motor mechanism of kinesin.

One challenge for *in vitro* measurements of motor proteins is collecting sufficiently high signals to allow for visualization. Total internal reflection fluorescence microscopy (TIRFM) provides a useful solution. In TIRFM, a laser beam is steered into a microscope objective at a high incident angle. Above a critical angle, the majority of the incident light is reflected, but a small portion propagates into the sample, parallel to the surface, as an evanescent wavefront that excites fluorophores on and near the surface [4]. This decreases the fluorescence emission from within the sample and increases the signal to noise ratio. By using two lasers of distinct wavelengths, kinesin and microtubules can be distinguished if labeled with two different fluorescent dyes that possess excellent photostability characteristics. The present study used an electron-multiplying charged coupled device (EMCCD) camera with the TIRFM system to provide fast, high-resolution data acquisition in order to characterize the velocity and photo-properties of fluorescent kinesin proteins.

## **Experimental Procedure:**

A protein expression protocol was developed and used to generate recombinant kinesin proteins. *Escherichia coli* bacteria, containing a plasmid with the *kif5b* kinesin gene fused to green fluorescent protein (GFP) for visualization and a histidine tag for purification, were obtained and replicated. This multi day procedure required sterility and ideal temperature and chemical conditions. After growth, cells were lysed by sonication, releasing cellular contents into solution. Kinesin was column purified using a type of nickel resin, which had high affinity for the histidine-tagged kinesin. Expression products were analyzed with gel electrophoresis.

Gliding filament assays were used to characterize the recombinant kinesin. Coverglasses were coated with GFP antibodies to bind kinesin to the surface. Because the GFP is located at the tail, each motor head pointed up into solution and attached and detached to microtubules in solution, thus causing them to glide. A 532 nm laser and a custom TIRFM system were used to visualize microtubules labeled with rhodamine dye.

For each microtubule, 200 frames were collected at a frequency of 10 frames per second with an EMCCD camera. Analysis software was implemented to locate the coordinates of the tip of each microtubule in the first and last frame (Figure 1). The distance between these points was calculated and divided by the elapsed time (20 seconds) to obtain velocity data. To assess photostability, single kinesin-GFP molecules were observed using a 473 nm laser.

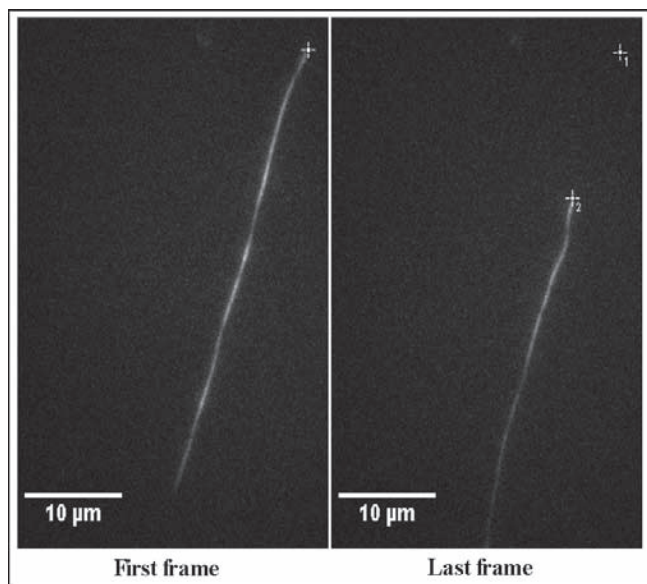


Figure 1: Analysis of a microtubule gliding assay video.

### Results and Conclusions:

Green protein fractions and gel electrophoresis confirmed that GFP-fused kinesin was successfully made. To assess the functionality, microtubule velocities were calculated via gliding assays. The velocities of 160 microtubules were measured to be  $650 \pm 80$  nm/s, consistent with earlier reports [5,6]. The distribution (Figure 2) was slightly skewed toward lower velocities, perhaps indicating the presence of non- or partly-functional motor proteins or imperfect surface immobilization.

Kinesin motors were also visualized at the single molecule level, and the fluorescence intensity was measured as a function of time to assess dye lifetime and brightness. The lifetime of a single GFP molecule was found to be  $\sim 10$  seconds, as indicated by the steep vertical drop in mean intensity (Figure 3). This singular drop confirmed that single molecule signal detection had been achieved.

### Future Work:

The robust protocol for the expression and characterization of kinesin motors that was developed will enable future analysis of a wide variety of motor proteins. In order to further improve the procedure, optimal conditions for single molecule imaging to reduce photobleaching, without impairing kinesin's functionality, should be investigated. Significant insight into the biology of motor proteins will be gained, which will help develop the promising concept of making proteins with desirable properties for cancer and disease applications.

### Acknowledgements:

Thank you to the National Nanotechnology Infrastructure Network Research Experience for Undergraduates Program and the National Science Foundation for funding my summer research. Special thanks to Dr. Megan T. Valentine, Dezhi Yu, Nikki Lapointe, Claudia Gottstein, Angela Berenstein, the members of the Valentine lab, and my friends and family for their guidance and support.

### References:

- [1] Mazumdar, M and Misteli, T; Trends Cell Biol. 15, 349-355 (2005).
- [2] Valentine, M and Gilbert, S; Curr. Opin. Cell. Biol. 19, 75-81 (2007).
- [3] Asbury, C; Curr. Opin. Cell. Biol. 17, 89-97 (2005).
- [4] Axelrod, D. et al; Ann. Rev. Biophys. Bioeng. 13, 247-368 (1984).
- [5] Rosenfeld, S. et al; J. Biol. Chem. 278, 18550-18556 (2003).
- [6] Romberg, L. et al; J. Cell Biol. 140, 1407-1416 (1998).

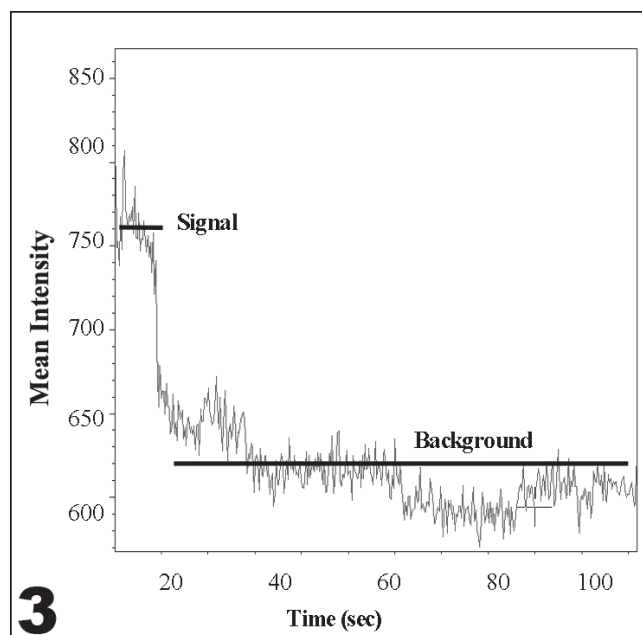
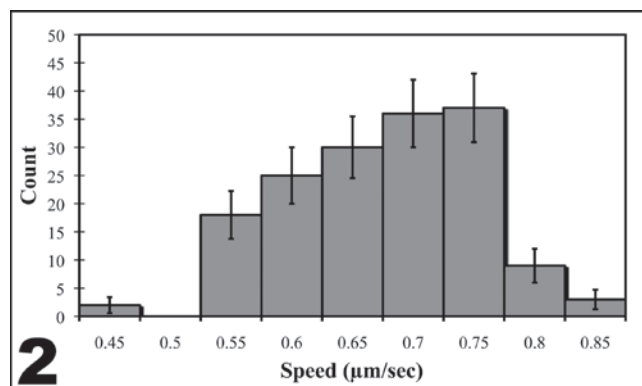


Figure 2, top: Distribution of microtubule speeds on kinesin-coated surfaces.

Figure 3, bottom: Photobleaching trace of a single GFP kinesin.

# Microfluidics Guided Self-Assembly of Magnetoliposomes

Tiffany Moeller

Chemical Engineering, University of Nebraska

**NNIN REU Site:** Cornell NanoScale Science and Technology Facility, Cornell University, Ithaca, NY

**NNIN REU Principal Investigator(s):** Carl Batt, Department of Food Science, Cornell University

**NNIN REU Mentor(s):** Matthew Kennedy, Dickson Kirui, Department of Food Science, Cornell University

**Contact:** tiffanymoeller@msn.com, cab10@cornell.edu, mjk67@cornell.edu, dk322@cornell.edu

## Abstract:

Liposomes in the range of 100 to 500 nm were created using a microfluidic flow-focusing device by varying composition and flow rates of the lipid and sheath fluids. Due to their amphiphilic structure, liposomes can be engineered to encapsulate magnetic nanoparticles, forming magnetoliposomes. The project aims were to (1) optimize reagent parameters to modify liposome size and (2) encapsulate nanoparticles. A three-dimensional microfluidic focusing manifold was employed to enhance the liposomes' monodispersity to improve *in vivo* pharmacokinetics. At flow rate ratios (FRRs)—sheath to lipid solution—from 10 to 25, increasing phospholipid concentration from 0.10 to 10.0 mM decreased liposome size from 215 to 120 nm. At the same FRRs, increasing the concentration of potassium chloride from 0.10 to 10.0 mM in the sheath fluid increased the liposomes' size from 120 to 470 nm; liposomes aggregated at FRRs less than 10.0. Magnetoliposomes were formed via an *in situ* precipitation of magnetite in the interior compartment of the liposomes.

## Background:

Monodisperse liposomes are more desirable for *in vivo* applications because they display more uniform pharmacokinetics [1,2]. Additionally, liposomes with diameters of 150 to 200 nm demonstrate prolonged circulation half-lives and more efficient extravasation of tumor microvasculature compared to liposomes of other sizes [3,4]. Therefore, microfluidic-directed formation of liposomes is very useful as it allows for controlled size and more monodisperse liposomes over other synthesis methods [4].

Magnetoliposomes have been engineered to encapsulate magnetic nanoparticles to concentrate therapeutics at the delivery site [4]. An alternating magnetic field can induce hyperthermia, allowing a burst-release of the encapsulated therapeutic [2]. Magnetoliposomes have been synthesized using other methods [5], but we employed the microfluidic platform to produce more monodisperse product of controlled size.

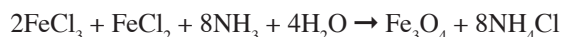
## Experimental Procedure:

**Microfluidic Device.** The microfluidic device was fabricated using general photolithography techniques. Polydimethylsiloxane (PDMS) was spun onto SU-8 patterned wafers, and the two pieces of PDMS were aligned. The cross-sectional dimensions of the square microchannel were 125  $\mu\text{m}$ ; the channel was 2.0 cm in length.

**Liposomes for Size Experiments.** The phospholipids 1,2-dipalmitoyl-*sn*-glycero-3-phosphocholine (DPPC) and 1,2-distearoyl-*sn*-glycero-3-phosphoethanolamine-N-[amino(polyethylene glycol)-2000] (DSPE-PEG) were dissolved with cholesterol (Chol) in ethanol in a 10.1:1.0:9.9

(DPPC/DSPE-PEG/Chol) molar ratio. The sheath fluid was deionized water or a potassium chloride solution. A syringe pump flowed the lipid solution through the center input of the device and the sheath fluid in the remaining four inputs. Product was collected at varying flow rate ratios (FRRs)—sheath to lipid solution—with a constant bulk flow rate of 20.39  $\mu\text{L}/\text{min}$  and a Reynolds number of 2.72.

***In situ* Synthesis of Magnetoliposomes (MLs).** The sheath fluid was 5.0 mM  $\text{FeCl}_3$  and  $\text{FeCl}_2 \cdot 4\text{H}_2\text{O}$  (2:1 molar ratio). The lipid solution (10.1:1.0:8.1; DPPC/DSPE-PEG/Chol) was pumped at 1.3  $\mu\text{L}/\text{min}$  and the sheath at 4.8  $\mu\text{L}/\text{min}$  (FRR = 14.7).  $\text{NH}_4\text{OH}$  solution was added to the liposomes to precipitate magnetite ( $\text{Fe}_3\text{O}_4$ ) according to the following chemical reaction:



**Size Determination.** Hydrodynamic radii were determined with dynamic light scattering (DLS) at 0.010 mM phospholipid concentrations. Measurements were taken at 90° with a Melles Griot HeNe 632.8 nm laser.

**Characterization by Transmission Electron Microscopy (TEM).** A 5.0  $\mu\text{L}$  aliquot of sample was pipetted onto a carbon-coated 200 nm mesh copper grid and stained with 5.0  $\mu\text{L}$  of sodium phosphotungstate negative stain. Images were taken with a Philips Tecnai T-12 scope at 120kV.

## Results and Discussion:

**Monodispersity of Liposomes.** The microfluidic device was based upon Kennedy et al. [6]. The three-dimensional design focused the lipid solution to the microchannel's

center. Diffusion of the lipids into the surrounding aqueous sheath fluid directed liposome self-assembly. Doing so narrowed the velocity distribution of the molecules, potentially narrowing the size distribution of the liposomes as well.

**Effect of FRR on Liposomes.** At FRRs below 10.0, there was no trend in liposome size (Figure 1). An insufficient volume of sheath fluid in the microchannel prevented complete diffusion of the lipids, resulting in incomplete liposome assembly. At FRRs of 10.0 and above, increasing the phospholipid concentration from 0.10 to 10.0 mM decreased liposome diameter from 215 to 130 nm. At the higher concentration, lipids had a shorter diffusion time before reaching the critical aqueous concentration at which liposomes self-assemble, resulting in smaller liposomes.

Increasing the sheath's salt concentration from 0.10 to 10.0 mM increased the liposomes from 150 to 470 nm. At the lower salt concentration, the solvating action of the water molecules stabilized the liposomes thereby minimizing their size. With increasing ionic strength, water molecules increasingly solvated salt ions. The instability created by decreased solvation resulted in larger liposomes which are prone to aggregation (Figure 2). Characterization by TEM showed all liposomes to be generally spherical; however, lipid aggregates predominated most samples (Figure 3).

**Characterization of Magnetoliposomes (MLs).** TEM images before and after addition of  $\text{NH}_4\text{OH}$  verified encapsulation of magnetite. Before  $\text{NH}_4\text{OH}$  addition, the liposomes were spherical with an average mean diameter of 160 nm. Precipitated magnetite appeared as black spots in the liposomes' interior (Figure 4). TEM verified DLS size measurements.

**Acknowledgments:**

The author thanks the National Nanotechnology Infrastructure Network Research Experience for Undergraduates (NNIN REU) Program and the National Science Foundation (NSF), the Cornell NanoScale Science and Technology Facility (CNF) and program coordinators Melanie-Claire Mallison and Rob Ilic, as well as the Batt Group—especially Matthew Kennedy, Dickson Kirui, and Carl Batt—for their assistance and support.

**References:**

[1] Xu, Q., et al.; Small Journal, 5.13, 1575-1581 (2009).  
 [2] Arruebo, M., et al.; Nanotoday, 2.3, 22-32 (2007).  
 [3] Litzinger, D., et al.; Biochimica et Biophysica Acta, 1190, 99-107 (1994).  
 [4] Gu, F., et al.; Nanotoday, 2.3, 14-21 (2007).  
 [5] Sabaté, R., et al.; International Journal of Pharmaceutics, 347, 156-162 (2008).  
 [6] Kennedy, M., et al.; "A Microfluidic Hydrodynamic Diffusion Mixer with Reduced Taylor Dispersion"; (2009).

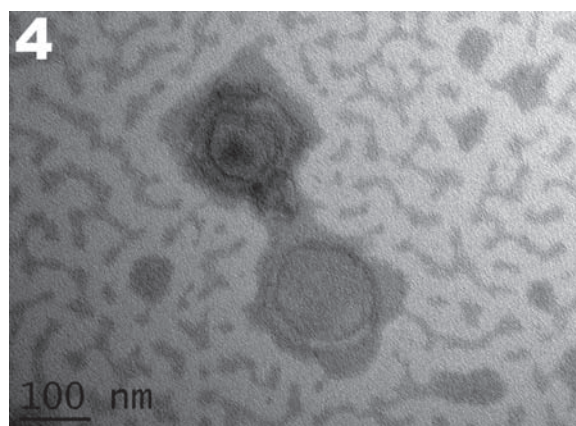
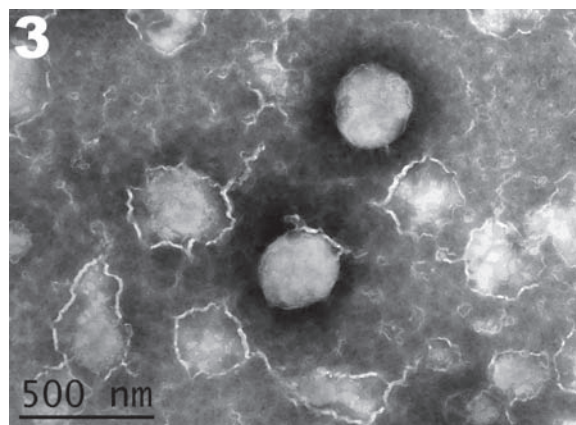
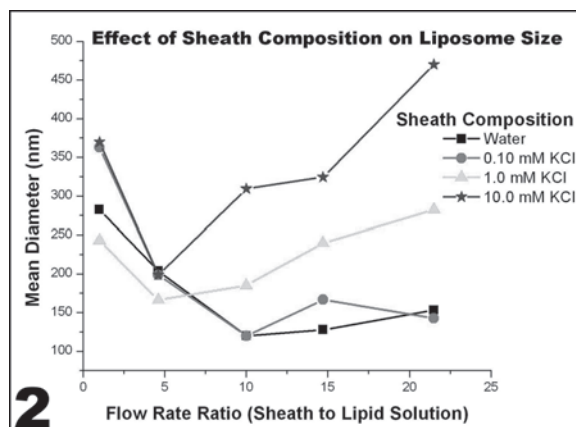
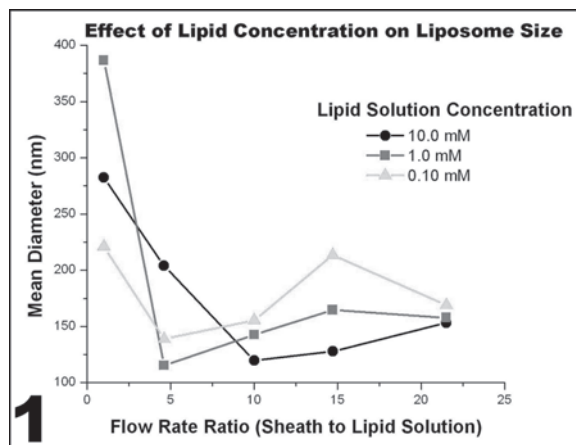


Figure 1: Increasing phospholipid concentration resulted in smaller liposomes.

Figure 2: Increasing ionic strength of the sheath fluid resulted in larger liposomes.

Figure 3: TEM image of liposomes with a mean diameter of 240 nm.

Figure 4: TEM image of a magnetoliposome. The top liposome is encapsulating magnetite while the bottom liposome is not.

# Using Molecular Self-Assembly for Surface Charged Monolayers to Control Bio-Assembly

Theresia Monikang

Chemistry Department, Hampton University

NNIN REU Site: Howard Nanoscale Science and Engineering Facility, Howard University, Washington, DC

NNIN REU Principal Investigator(s): Dr. James Mitchell, Materials Chemistry and Engineering, Howard University

NNIN REU Mentor(s): Dr. Tina Thomas Brower, Chemistry, Howard University

Contact: Chemdance@yahoo.com, Theraneh@yahoo.com

## Abstract/Introduction:

Self-assembled biological molecules are being utilized in many ways to include forming hydrogel networks and nanoscale tubes. The goal of this project is to develop a method to preferential assembly biomaterial on surfaces using ionic interactions. We employ photolithography and prepare a simple pattern—an array of gold (Au (111)) on mica. We form a monolayer of 4, 4'-dimercaptobiphenyl on the Au (111) surface. The monolayer is then treated with a photoresist, followed by selective exposure leaving part of the monolayer inaccessible. The monolayer is exposed to a solution of mercury (II) per chlorate hydrate. The mercury (II) per chlorate provides a positive charge to exposed area of the patterned surface. Finally the array is introduced to various biomaterials with the expectation that localized ionic interactions will result in preferential assembly of biomaterial. The array is examined by Kelvin force microscopy (KFM) before and after their introduction to the biomaterial.

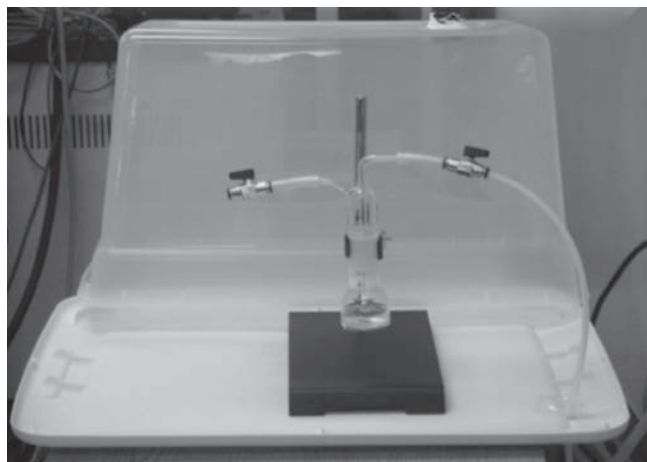


Figure 1: Homemade vented box. The bubbler flask is connected to a nitrogen gas tank allowing the self-assembly to occur in a nitrogen atmosphere.

## Experimental Procedure:

The experiment was performed under a homemade vented box (Figure 1). The box contained a bubbler flask that was connected to a nitrogen tank. It was important for the solutions to be in a nitrogen atmosphere in order to prevent the formation of dual mechanism bifunctional polymer (DMBP) via disulfide bonds. Therefore, all the glassware were cleaned using a piranha solution. Cleanliness was important because impurities could interfere with the formation of a monolayer.

A 1  $\mu\text{M}$  solution of DMBP was prepared and introduced to the bubbler flask. A gold sample was obtained and cleaned using an argon plasma. After cleaning the substrate, the optical constants were obtained using ellipsometry. These optical constants were later used to find the thickness of the monolayer. After measuring the optical constants, the substrate was put into the bubbler flask containing DMBP and left to self-assemble for four hours (Figure 2). After self-assembly, the gold substrate was rinsed with 200 proof ethanol and dried with a stream nitrogen gas. The monolayer thickness was obtained using ellipsometry.

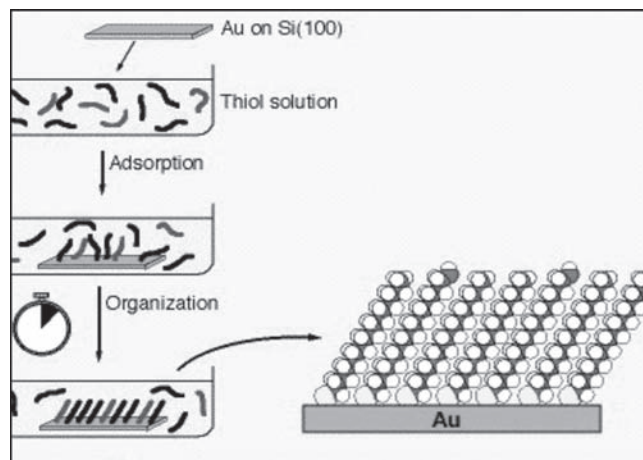


Figure 2: Gold substrate is put into a DMBT solution, DMBT self-assembles onto Au (111) substrate in a four hour period, to form a monolayer. Ref. <http://www.ifm.liu.se/applphys/jtir/sams.html>.

A pattern of 103  $\mu\text{m}$  squares was created on a gold substrate using photolithography. A small area was covered with photoresist and left un-etched, leaving that part of the substrate available for measuring the thickness of the monolayer. The previous procedure was repeated to make the monolayer, then positive charges were partially introduced to the monolayer surface using mercury (II) per chlorate. In order to have a partially charged monolayer surface, half of the gold substrate was covered with photoresist. The photoresist was meant to keep the positive charges absent from certain areas. The charges were exposed in areas with no photoresist. The bubbler flask contained 50  $\mu\text{M}$  of mercury (II) per chlorate in 50/50 200 proof ethanol in distilled  $\text{H}_2\text{O}$ . It seemed the photoresist adhered to the substrate well with 50/50 ethanol in distilled  $\text{H}_2\text{O}$ . After the two hour duration, the partially charged monolayer was taken out of the flask and analyzed using an atomic force microscopy — Kelvin force microscopy method, AFM/ KFM.

The maximum scan range for the AFM/KFM is 100  $\times$  100  $\mu\text{m}$  while our Au substrate was 1  $\times$  1 cm. Therefore we double-masked the substrate so that each 103  $\mu\text{m}$  square on the pattern had one half with a DMBP monolayer and the other half with a DMBP monolayer that had been exposed to mercury (II) perchlorate hydrate. This procedure rendered the sample a useful size for measuring by AFM. Biomaterial with inherent negative charges was then introduced to the partially charged monolayer surface.

**Results:**

After cleaning with the argon plasma, the optical constants obtained were  $N_s = 0.186$  and  $k_s = 3.400$ . The average thickness of the monolayer was 14.90 $\text{\AA}$ . After the two hour time duration of creating the partially charged monolayer, the substrate no longer had photoresist on certain areas. Using a different approach, 50/50 ethanol in distilled  $\text{H}_2\text{O}$  was used. It seemed the photoresist adhered to the substrate well with 50/50 ethanol in distilled  $\text{H}_2\text{O}$ . Photolithography was used to double mask the substrate. The size of the substrate was initially too big to measure by AFM/KFM. For this reason, a partially charged monolayer was made on each of the patterned squares as an alternative to using the entire substrate (Figure 3). The biomaterials exposed to the partially charged monolayer included red blood cells, cellulose, and sulfuric acid in cellulose. Unfortunately the biomaterials did not preferentially adhere to the positive charges on the

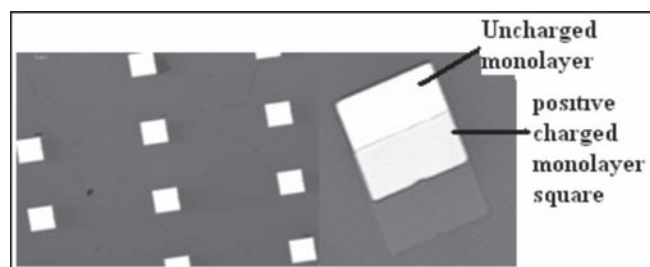


Figure 3: Patterned monolayer substrate (on left). Double patterned partially charged square (on right).

monolayer (Figure 4). The biomaterials covered the entire surface of the substrate.

**Conclusion:**

We successfully created a patterned surface of 102  $\mu\text{m}$  gold squares using photolithography. We were also successfully in preparing a single monolayer of DMBP on Au (111). In addition, we developed a method to selectively place charges on a monolayer. However, we did not show preferential adhesion of biomaterials to the positively charged areas of the monolayer.

Future work will include using other biomaterials in proving preferential assembly to charged surfaces. Finally, the continued study of the surfaces by AFM/KFM will be pursued in an effort to improve the patterning of the surfaces.

**Acknowledgments:**

I would like to thank the National Science Foundation, the NNIN REU Program, and HNF staff for the internship opportunity this summer. A special thanks to my principal investigator Dr. James Mitchell and my mentor Dr. Tina Thomas Brower for guiding me and making my first research experience enjoyable. I also wish to thank site coordinator Mr. James Griffin for his guidance and support.

**References:**

- [1] Brower, L.T. "SA Multilayer of 4, 4'-Dimercaptobiphenyl Formed by CU (II)-Catalyzed Oxidation." 18-16 Nov. 2002: 6207-6216.
- [2] Jordon, R., A. Ulman, J.F. Kang, S. Liao. "Mixed Self-assembled Monolayers of Rigid Biphenyl Thiols: Impact of Solvent and Dipole Moment." 120-8 April 1998: 9662-9667.
- [3] Dickie, D.A., Chan, A.Y.C., Jalali, H., Jenkins, H.A., Yu, H.-Z., Clyburne, J.A.C. "*m*-Terphenyl thiols: rigid and bulky molecules for the formation of bioactive SA monolayers on gold"; Chem. Comm., 2004 2432-2433.
- [4] Kane RS, Takayama S, Ostuni E, Ingber DE, Whitesides GM., "Patterning proteins and cells using soft lithography"; Biomats 20 (1999)2363-2376.

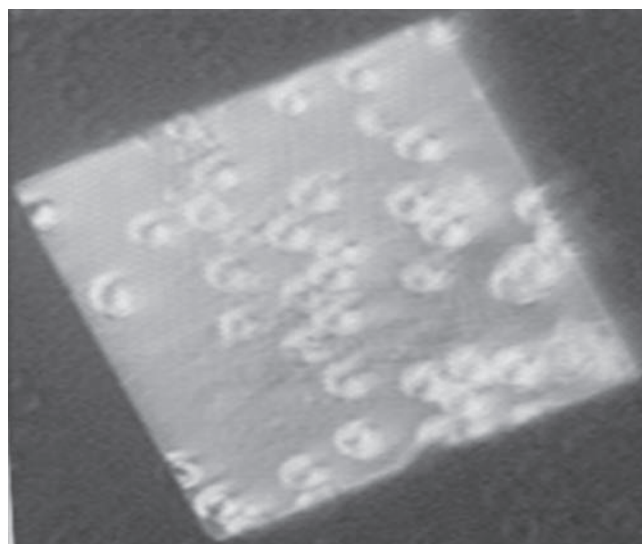


Figure 4: Blood cells did not seem to have a preference on the partially charged monolayer when exposed to the squares on the surface. In the picture above, the cells adhere to the whole square.

# Engineering Hcp1 to Bind DNA

Keith Olson

Biochemistry and Psychology, Beloit College

**NNIN REU Site: Center for Nanotechnology, University of Washington, Seattle, WA**

*NNIN REU Principal Investigator(s): Dr. Joseph Mougous, Microbiology, University of Washington-Seattle*

*NNIN REU Mentor(s): Julie Silverman, Department of Microbiology, University of Washington-Seattle*

*Contact: olsonk@stu.beloit, mougous@u.washington.edu, silverjm@u.washington.edu*

## Introduction:

Proteins are appealing building blocks for nanoscale systems because they are inexpensive, biocompatible, and have self-assembling properties. Specifically, protein nanotubes, such as viral capsids, microtubules, and tobacco mosaic viruses have been engineered for nanotechnological applications including nanowire synthesis, drug delivery, and gene delivery [1-3].

Current deoxyribonucleic acid (DNA) processing methods used for DNA sequencing and microarray analysis rely on restriction enzymes that produce oligonucleotides of heterogeneous lengths. Homogenous length DNA would be an advantage to chip based DNA analysis technologies as a way to reduce false positives (incorrect matches of complementary DNA). Nanotubes of discrete lengths could serve as a template for length specific DNA processing.

Our lab has previously demonstrated that Heme Carrier Protein 1 (Hcp1), a homohexameric ring protein secreted by *Pseudomonas aeruginosa*, forms stable nanotubes [4]. Currently, our lab is focused on optimizing Hcp1 to form tubes of discrete length. The potential to control nanotube length makes Hcp1 an ideal candidate for DNA scaffolding applications.

In this study we report progress toward DNA encapsulation with Hcp1. The work presented here, shows that the introduction of positively charged lysines to the interior of Hcp1 can mediate non-specific interactions between Hcp1 and the negatively charged backbone of DNA.

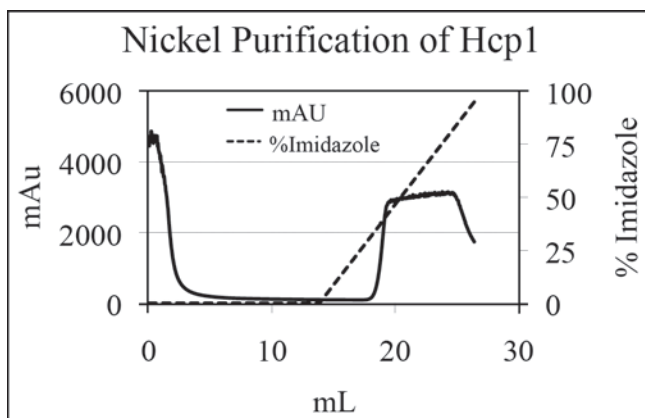


Figure 1: Representative elution profile of Hcp1 lysine mutants.

## Materials and Methods:

**Lysine Mutant Production and Purification.** We produced two lysine modified Hcp1 mutants—Asp55Lys and Ser31Lys Asp55Lys—via site-directed mutagenesis. Hcp1 mutants were expressed in *E. coli* and purified over a His-Trap column with an increasing concentration gradient of imidazole buffer and were further purified on a size exclusion column.

**Hcp1-DNA Electrophoretic Mobility Shift Assay.** 1  $\mu$ M of 40 base pair (bp) DNA and various protein concentrations of Hcp1 wild type Hcp1 (WT), Hcp1 (Asp55Lys) and Hcp1 (Ser31Lys Asp55Lys) mutants were mixed and incubated for one hour on ice. Next, the reactions were run on a 2% TBE agarose gel at 50 V for two hours, stained with ethidium bromide, rinsed and photographed using UV imaging. The second electrophoretic mobility shift assay (EMSA) incubated 100 nM plasmid DNA with various concentrations of Hcp1 WT, Hcp1 Asp55Lys and Hcp1 Ser31Lys Asp55Lys for 1 hour on ice. The mixtures were run on a 1.5% gel for 4 hours at 50 V, stained with ethidium bromide, rinsed and visualized by UV transillumination using a gel documentation system.

**TEM Analysis of Hcp1 Asp55Lys with Cysteine Modifications.** Hcp1 lysine mutants with engineered cysteine residues were produced and proteins purified as previously described. Protein samples were stained with uranyl formate and imaged by transmission electron microscopy (TEM).

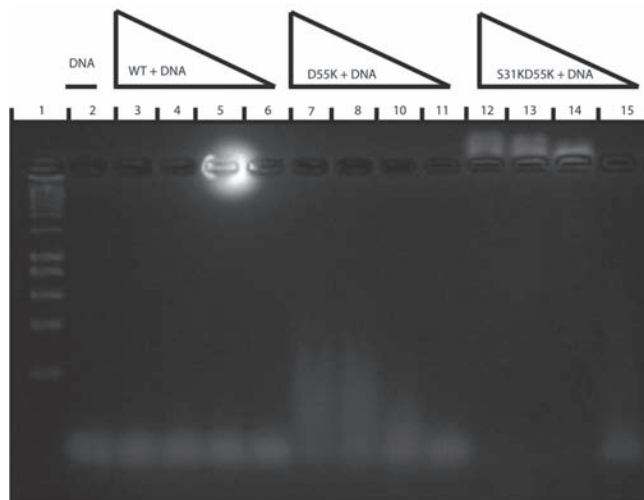


Figure 2: EMSA of DNA in the presence of Hcp1.

**Results:**

**Hcp1-DNA EMSA.** We performed electrophoretic mobility shift assays (EMSA) to determine if Hcp1 mutants would bind DNA with greater affinity than the WT. Figure 2 shows varied concentrations of Asp55Lys and Ser31Lys Asp55Lys in the presence of a 1  $\mu$ M 40 base pair (bp) DNA strand. (Lane 1, DNA Ladder; lane 2, DNA control, lanes 3-6, lanes 7-11 and lanes 12-15 contained WT, Asp55Lys and Ser31Lys Asp55Lys respectively) (10  $\mu$ M, 7  $\mu$ M, 4  $\mu$ M and 1  $\mu$ M). At high concentrations of Asp55Lys and low concentrations of Ser31Lys Asp55Lys, a smear of DNA is observed, which is not seen with the WT. At high protein concentrations, Ser31Lys Asp55Lys shifts in the slightly positive direction. Additionally, low concentrations of Ser31Lys Asp55Lys weaken the DNA band compared to the DNA control.

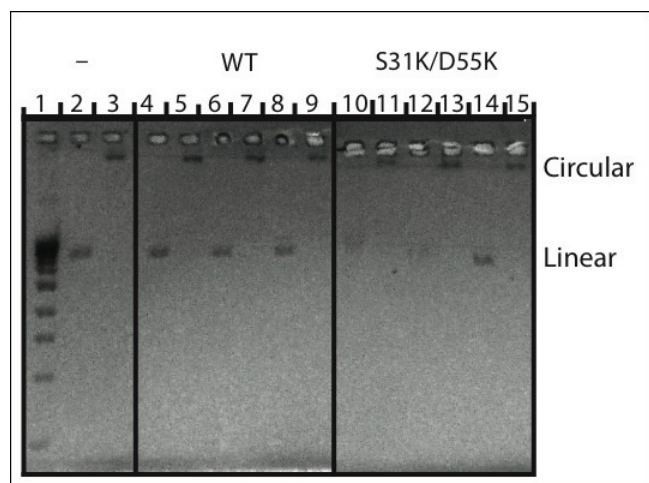


Figure 3: EMSA of circular vs. linear plasmid DNA.

**Linear vs. Plasmid DNA EMSA.** We utilized an EMSA with circular and linear plasmids to determine if DNA was binding to the interior of the protein. Figure 3 shows Ser31Lys Asp55Lys altered DNA migration patterns of the linear plasmid but not the circular plasmid. Protein concentration decreased left to right; 8  $\mu$ M, 4  $\mu$ M, 1  $\mu$ M in lanes 1 and 2, 3 and 4, and lanes 5 and 6 respectively. The linear DNA shifted at high concentrations of Ser31Lys Asp55Lys.

**TEM Hcp1 Asp55Lys with Cysteine Modifications.** Transmission electron microscopy (TEM) visually confirmed Hcp1 Asp55Lys tube formation as previously described by Ballister et. al. [4] (Figure 4).

**Discussion:**

This work demonstrates the preliminary steps towards producing DNA encapsulating tubes. We show the introduction of positively charged lysine to the interior of Hcp1 promotes a non-specific DNA-protein interaction. At high concentrations of Ser31Lys Asp55Lys, an upward shift indicates a positively charged and possibly large DNA-protein complex. However, these results may suggest an aggregated complex of DNA and misfolded protein. Similarly, DNA smears can stem from a variety of possibilities including DNA being released during electrophoresis, numerous

complexes forming and the presence of various charged species. Therefore, this experiment is inconclusive.

Preliminary evidence suggests DNA is binding to the interior of Hcp1. First, the protein eluted at the volume expected for the hexamer (data not shown). The linear plasmid migration pattern was altered in the presence of Ser31Lys Asp55Lys whereas the circular plasmid did not appear to show shift (Figure 3). This suggests DNA is binding to the interior of the protein because the linear DNA has exposed ends to allow for binding to the interior of Hcp1. This evidence depends on stable ring formation, which has not been conclusively determined yet. Although clear evidence of stable ring formation is not available for the Ser31Lys Asp55Lys mutant, we did observe intact ring conformation and tube formation for Asp55Lys (Figure 4).

Future steps include imaging the interaction between Hcp1 mutants and DNA encapsulation for tubes. The introduction of a di-copper complex at the top and bottom of an Hcp1 tube could cut DNA based on tube length. Di-metal complexes have shown to non-specifically cut the backbone of DNA5. This system would serve as an excellent scaffold to synthesize homogenous length DNA strands.

**Acknowledgements:**

I would like to thank Julie Silverman, Dr. Joseph Mougous, the Nanotechnology Infrastructure Network Research Experience for Undergraduates Program and National Science Foundation for funding.

**References:**

- [1] Lamber, O, Letellier L, Gelbart WM, Rigaud JL; "DNA delivery by phage as a strategy for encapsulating toroidal condensates of arbitrary size into liposomes"; J Gen Virol 81, 2531-2543 (2000).
- [2] Cooper, A., Shaul, Y; "HBV viral capsid"; Biophysical and Biochemical Research Communications, 327, 1094-1099 (2005).
- [3] Wang, Y, Schwedes, J, Mann, K, Tegtmeyer, P; "Interaction of p53 with its consensus DNA-binding site"; MolCellBio, 15, 1094-99 (2000).
- [4] Ballister, E., et al.; "In vitro self-assembly of tailorable nanotubes from a simple protein building block"; Proc Natl Acad Sci USA, 105, 3733-3738 (2008).
- [5] Rey, N., et al.; "Catalytic Promiscuity in Biomimetic Systems: Catecholase-like Activity, Phosphatase-like Activity, and Hydrolytic DNA Cleavage Promoted by a New Dicopper(II) Hydroxo-Bridged Complex"; Inorg. Chem., 46, 348-350 (2007).

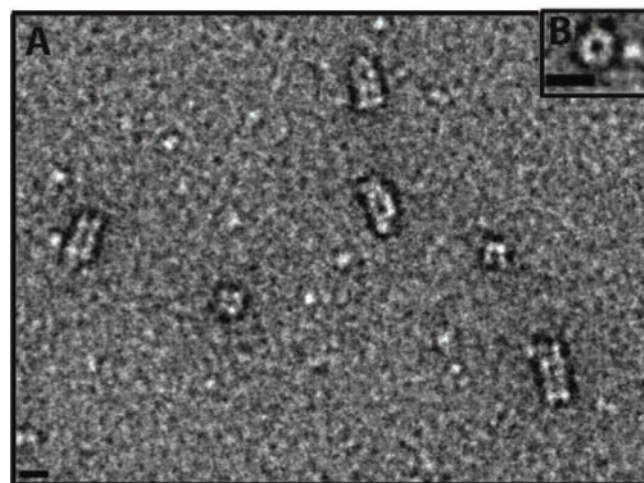


Figure 4: TEM of Hcp1 D55K with cysteine modifications.

# Nano-Magnetic Particles for Cancer Diagnostics

Barbara D. Raynal

Electrical Engineering, University of Notre Dame

**NNIN REU Site: Stanford Nanofabrication Facility, Stanford University, Stanford, CA**

*NNIN REU Principal Investigator(s): Prof. Shan X. Wang, Materials Science and Electrical Engr, Stanford University*

*NNIN REU Mentor(s): Mingliang Zhang, Robert Wilson, Materials Science, Stanford University;*

*Dr. Mary Tang, Stanford Nanofabrication Facility, Stanford University*

*Contact: braynal.at.nd.edu, sxwang.at.stanford.edu, mzhang2@stanford.edu,*

*bobmse@stanford.edu, mtang@stanford.edu*

## Abstract:

Nano-magnetic particles can be used to detect cancer cell markers in biological fluids. Cancer proteins are tagged with magnetic particles to identify cancer proteins since magnetism is rare in biological systems. The objective of this work was to create nano-magnetic particles of varying sizes that could be used to study the detection of different kinds of cancer cells. First, a monolayer of polymer nanospheres was spincoated onto a silicon wafer. The nanospheres were then etched and used as a mask to create a template consisting of tiny pillars. A second silicon wafer was then coated with polymethylglutarimide (PMGI) and polymethylmethacrylate (PMMA). The template was imprinted onto the PMMA layer of the second wafer to create many holes the size of the pillars. Next, the PMGI layer was etched with LDD26W to create deeper holes, followed by metal deposition. The metal fell into the holes and nanoparticles the size of the etched nanospheres were created. By varying the etching parameters it was possible to create templates with different pillar size, and by using one of the templates it was possible to create nanoparticles with the purpose of facilitating the detection of different kinds of cancer cells.

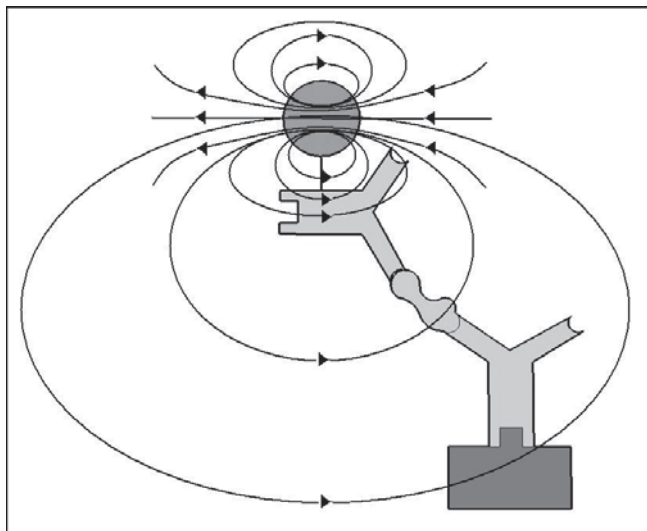


Figure 1: Sensor detecting the magnetic field of the nano-particle.

## Introduction:

A silicon chip was embedded with sensors that were coated with different kinds of antibodies. When the blood sample was added, the antibodies grabbed specific cancer related proteins. A solution of nano-magnetic particles attached to antibodies was then added. The added antibodies attached to the captured proteins and a large external magnetic field was applied, which caused the nano-particles to create a stronger

magnetic field. If the magnetic field created by the particles was detected by the sensor, it meant cancer related proteins had been found. Figure 1 is a good representation of how the device worked.

The nano-particle was made of five alternated layers of titanium and iron. The purpose of the surface layers of titanium was to prevent the iron layers from oxidizing. The iron layers created magnetic moments which pointed in opposite directions when no external magnetic field was applied so that the net magnetic field was zero. Because iron is a ferromagnetic element, the two layers could act as magnets when an external field was applied. The external field caused the opposing magnetic moments to gradually rotate until they were completely aligned with the external magnetic field, creating an even stronger one which was then detected by the sensor.

A self-assembly process was used rather than electron-beam lithography because the cost per unit area is about a thousand times less expensive for the self-assembly process.

## Experimental Procedure:

The first step was to create a mask. First, a silicon wafer was coated with a monolayer of polymer beads that were originally 320 nm in diameter. A mixture of chlorine and oxygen gas was then used for plasma etching on the polymer beads with a resulting diameter ranging from 50 to 200 nm.

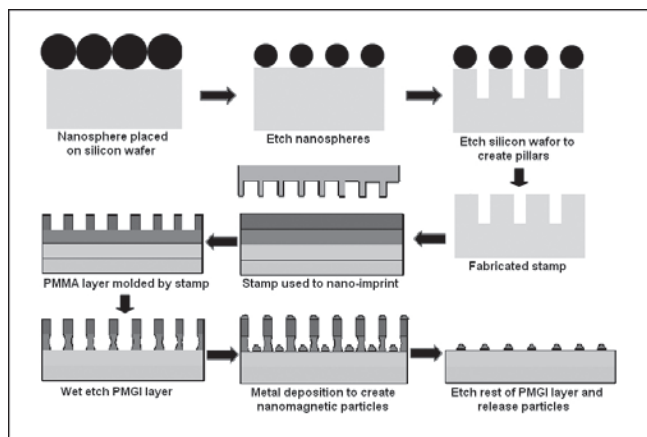


Figure 2: Nano-magnetic particle fabrication process.

The beads acted as a mask so that when the silicon was etched with a mixture of chlorine, hydrobromic acid, helium and oxygen gas, tiny pillars the size of the etched nanospheres were created. After the mask had been created, a second silicon wafer was coated with three polymer layers for the nano-imprinting step: the release layer, PMGI which was the undercut layer, and PMMA. The nano-imprinting was done at a temperature of 180°C. At this temperature, the PMMA layer became soft but the PMGI and release layers remained solid so that when pressure was applied on the wafers, only the PMMA layer was molded by the mask.

Once the mask was removed, tiny holes the size of the etched nano-spheres were left on the PMMA layer. LDD 26W was then used to wet etch the PMGI layer to create a deeper hole where the nano particle had deposited. Layers of iron and titanium were deposited into the holes through metal deposition. The rest of the PMGI layer was then etched and the nano-particles were left on the release layer, which was then dissolved in order to release the nano-particles. The fabrication process is represented in Figure 2.

**Results and Conclusions:**

Masks of different pillar size were created by varying the etching time. The polymer sphere etching was first done starting at 10 seconds up to 30 seconds with 5 second intervals in between. All of the samples turned out to be under etched except the 30 second etched sample. A few more masks were then made with different etching times centered at 30 seconds. Through this process of varying etching times, it was possible to successfully create two masks with optimal pillar dimensions for the creation of nano-magnetic particles at 27 and 29 seconds etching times for the polymer spheres, and a 35 second etch for the silicon wafer. The 27 second etched mask is shown in Figure 3. The diameter of the pillars is 120 nm and their height is 212 nm. A previously made mask using 390 nm polymer spheres was used to create nano particles through the nano-imprinting process. The particles are shown in Figure 4.

**Future Work:**

In the future, nano-particles will be created using the 27 and 29 second etched masks as well as working on finding ways by which the nano-magnetic particles can be attached to the antibodies.

**Acknowledgements:**

I would like to thank my mentors Mingliang Zhang, Dr. Mary Tang, Dr. Robert Wilson, my PI Prof. Shan X. Wang, our site coordinator Dr. Michael Deal, Maureen Baran and the SNF staff, the National Nanotechnology Infrastructure Network Research Experience for Undergraduates Program and the National Science Foundation.

**References:**

[1] S.J. Osterfeld, H. Yu, R.S. Gasataer, S. Caramuta, L. Xu, S.-J. Han, D.A. Hall, R.J. Wilson, S. Sun, R.L. White, R.W. Davis, N. Pourmand, and S.X. Wang. "Multiplex protein assays based on real-time magnetic nanotag sensing." PNAS vol. 105 no. 52 (2008): 20637-20640.

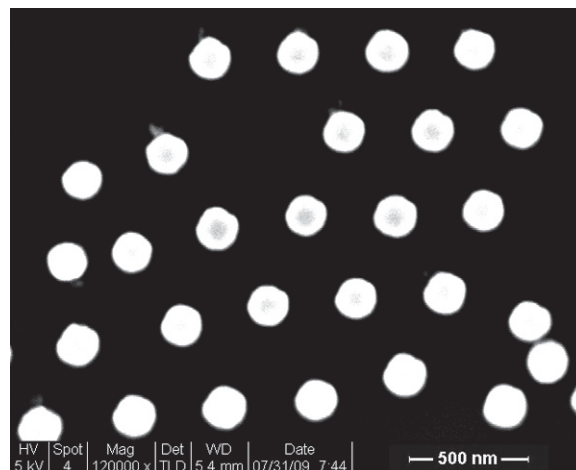
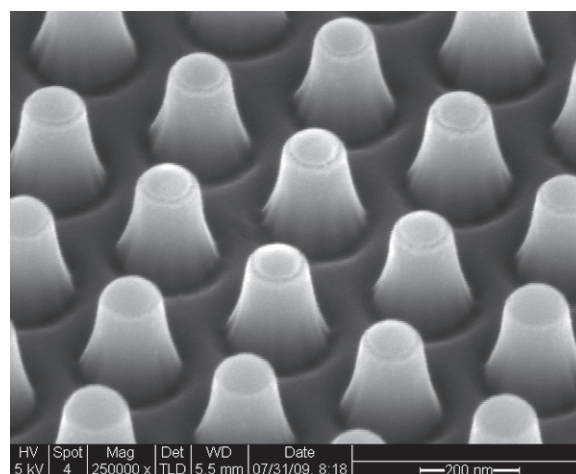


Figure 3, top: Resulting mask after a 27 second etch of the polymer nano-spheres.

Figure 4, bottom: Nano-magnetic particles created by nano-imprinting.

# Optimization and Bioconjugation of Silicon Nanowire Biosensors for Cancer Marker Detection

Jacob Sadie

Electrical Engineering, Clemson University

**NNIN REU Site: Nanotechnology Research Center, Georgia Institute of Technology, Atlanta, GA**

*NNIN REU Principal Investigator(s): Dr. James Meindl, Electrical Engineering, Georgia Institute of Technology*

*NNIN REU Mentor(s): Ramasamy Ravindran, Electrical Engineering, Georgia Institute of Technology*

*Contact: jake.sadie@gmail.com, james.meindl@misc.gatech.edu, rravindran@gatech.edu*

## Introduction:

Silicon nanowire (SiNW) biosensors are highly sensitive nanoscale field-effect transistors. Because the channel width and height are on the nanometer scale, minor environmental alterations elicit obvious changes in the transistor's conductivity [1]. With proper bioconjugation techniques, the presence of bound molecules in buffer solutions will alter the surface charge on the nanowires, changing the conductivity of the wire and indicating the sensing event [2]. Label-free methods are more cost and time-effective than labeled procedures, so we will focus our work on successful label-free procedures for ultimately detecting cancer markers [1]. Our process is a top-down fabrication technique including electron-beam lithography for the patterning of silicon nanowires. This project focused on optimizing the fabrication process by (a) adjusting the electron-beam resist application and etching procedures, (b) modifying the annealing procedures before and after electrode deposition, and (c) determining optimal conditions for pH sensing and protein bioconjugation.

## Procedure:

**Fabrication.** The fabrication process began with electron-beam lithography (EBL) using negative resist hydrogen silsesquioxane (HSQ) spun on a silicon-on-insulator (SOI) wafer. The pattern was an array of sixteen nanowires. After lithography, we developed the resist with resist developer MF-319. Next, dry plasma etching with a standard oxide etcher (SOE) removed both silicon and HSQ to expose the silicon nanowires (SiNW) and buried oxide layer (BOX). To optimize the resist procedure, the initial thickness of HSQ was found using an automated film thickness measuring system. By varying the initial thickness (~ 30-40 nm) and etch time (14-20 sec) and then using a profilometer to measure the final thickness, the etch rates of HSQ, silicon, and the BOX could be found. Next, an oxygen anneal in a rapid thermal processor (RTP) reduced damage caused by the etching process and grew an oxide layer on the SiNWs. Our wafers underwent optical lithography (NR9-1500PY resist) and electron-beam evaporation to pattern the aluminum electrode contacts. A final forming gas anneal was performed in the RTP to ensure contact between the SiNWs and aluminum

contacts. The time for this anneal was varied to determine the most effective procedure. A final passivation step exposed the tips of the aluminum electrodes and a small rectangular region around the nanowire array to prepare for wet testing.

**Testing.** Dry testing involved a three-point probe, where the source and drain were two electrodes on either end of the SiNW and the chuck acted as a back-gate. We used a semiconductor parameter analyzer to measure the drain current versus source drain voltage at varying gate voltages as well as the transconductance of the nanowires. To perform wet testing we attached glass wells around the exposed nanowire array using crystal bond. Then, buffer solutions at different pH levels were transferred in and out with a micropipetter. A third test was also performed, which plotted the transient drain current as buffer solutions in the well were changed.

**Functionalization.** The final procedure for protein conjugation required silicon nanowire functionalization with 3-aminopropyltriethoxysilane (3-APTES) [3]. We then bonded fluorophore-tagged (FITC) proteins to the 3-APTES molecules using a 2-(*N*-morpholino) ethanesulfonic acid (MES) buffer solution, a cross linker, and an activator.

## Results:

**Resist Optimization.** We were able to characterize the etch rates of HSQ, silicon, and BOX in our given plasma process (Figure 1). The most important etch rate determined was the HSQ etch rate. Previously, the initial HSQ thickness of the process was approximately 80 nm, which meant that even after a buffered oxide etch (BOE) dip, HSQ may have remained

Spin	Average HSQ Height After EBL (nm)			Standard Deviation (nm)		
1	41.6			0.9		
2	33.1			1.4		

Spin	Average Etch Rates (nm/s)			Standard Deviation (nm/s)		
	Si	BOX	HSQ	Si	BOX	HSQ
1	5.9	0.9	1.6	0.0	0.1	0.1
2	5.9	1.0	1.5	0.0	0.3	0.3
Cumulative	5.9	1.0	1.6	0.0	0.2	0.2

Figure 1: Silicon, buried oxide, and HSQ etch rates.

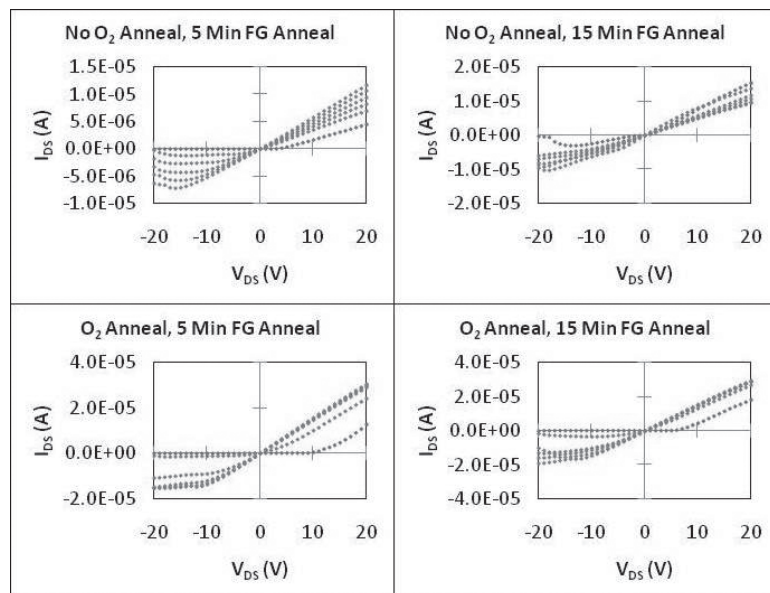
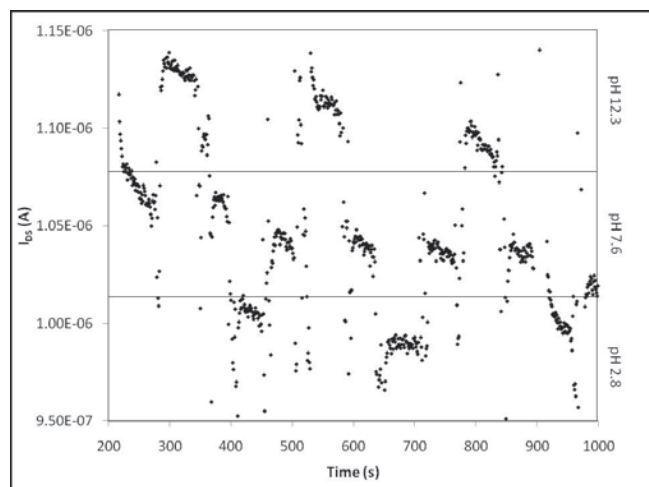


Figure 2, above: Anneal optimization results.

Figure 3, below: Transient pH test results.



on the SiNW and prevented bioconjugation. Now, we have optimized initial HSQ thickness to be approximately 40 nm, allowing the plasma etch to nearly remove all of the HSQ and ensuring complete removal after a short dip in BOE.

**Anneal Optimization.** Our tests altered the two anneal procedures to determine the most effective process before and after metallization. Results seen in Figure 2 reveal that the initial oxygen anneals prior to metallization proved necessary, as the drain current range was doubled as a result of this anneal. In addition, we determined that there is no significant difference between a five or fifteen minute post-metallization anneal with FG. Finally, energy dispersive spectroscopy (EDS) indicated that thirty minute FG anneals would sometimes cause the aluminum to diffuse the length of the SiNW, effectively creating short circuits.

**Potential of Hydrogen (pH) and Bioconjugation.** Figure 3 indicates that our chips can sense and function over a

range of pH levels. However, there was only an approximately 15% change in current over our large pH range rather than reported current changes of about 50% over similar pH ranges [3]. Finally, our bioconjugation techniques proved successful as seen in Figure 4. When performing a photobleaching process with confocal microscopy, we confirmed the binding of proteins to a silicon dioxide substrate.

**Future Work:**

The next steps will be to apply the bioconjugation techniques we have begun to the SiNW array in order to begin protein sensing experiments. Finally, because label-free methods are the ultimate goal, we will begin researching methods for label-free bioconjugation and testing.

**Acknowledgements:**

I would like to acknowledge Dr. James Meindl and Ramasamy Ravindran for granting me the opportunity to work on this project. In addition, I would like to thank the members of the GSI group for being so welcoming and the MiRC staff for providing a hospitable work environment. Finally, thanks to the National Science Foundation and the National Nanotechnology Infrastructure Network Research Experience for Undergraduates (NNIN REU) Program for funding.

**References:**

- [1] Stern E, "Label-free sensing with semiconducting nanowires" (PhD dissertation, Yale University, 2007) pp. 39-93.
- [2] Stern E, Vacic A, Reed MA, "Semiconducting Nanowire Field-Effect Transistor Biomolecular Sensors," IEEE Transactions On Electron Devices, vol. 55, pp. 3119-3130, Nov. 2008.
- [3] Cui Y, Wei QQ, Park HK, Lieber CM, (2001) "Nanowire nanosensors for highly sensitive and selective detection of biological and chemical species," Science 293:1289-1292.



Figure 4: Bioconjugated and photobleached SiO<sub>2</sub> substrate.

# Development of an Intravessel Xylem Probe for Viniculture and Forest Ecology

Ellen Sedlack

Microelectronic Engineering, Rochester Institute of Technology

NNIN REU Site: Cornell NanoScale Science and Technology Facility, Cornell University, Ithaca, NY

NNIN REU Principal Investigator(s): Abraham Stroock, Chemical and Biomolecular Engineering, Cornell University

NNIN REU Mentor(s): Amit Pharkya, Chemical and Biomolecular Engineering, Cornell University

Contact: exs2093@rit.edu, ads10@cornell.edu

## Abstract:

This research project presents the design, fabrication and testing of a single, hollow microneedle whose purpose was to be integrated with a water pressure sensor to form a microelectromechanical systems (MEMS) intravessel xylem probe (IVXP). The intent of this IVXP would be to continuously extract a fluid sample from plant xylem to monitor water content. Double polished silicon wafers were coated with photoresist, patterned via photolithography, and deep reactive ion-etched. The resultant matrix of various needle dimensions was diced to create individual needles, which then were characterized with grape vine xylem. Successful xylem insertion was observed for needles of 200  $\mu\text{m}$  in length.

## Introduction/Background:

Botanical research demands improved technology to measure water transport in the xylem tissue of plants. Initial methods were indirect as they measured, in surrogate, the water content of air and soil. Current lab-confined probes [1] yield a single measurement per puncture, are destructive to the plant tissue and suffer from a pressure limit of minus 10 atmospheres (atm).

As plant fluids function at relatively high negative pressures, this sap is metastable and defies easy extraction; this liquid readily changes phase from liquid to gas, which sabotages analysis. The design of this project's *in situ* probe, inserted into xylem, would continuously read water flow in a growing plant and would provide readings down to minus 80 atm. A micro-proportioned needle could traverse the short distance into the xylem but without causing plant mortality.

The smaller needles feature a 20  $\mu\text{m}$  inner diameter and a 30  $\mu\text{m}$  outer diameter. The largest needles feature a 40  $\mu\text{m}$  inner diameter and a 100  $\mu\text{m}$  outer diameter. Recent micro-needle research and development [2] has etched needles as arrays, because, due to strength in numbers, these needles are less submissive to fracture. However, this project required a single needle strong enough to survive xylem probing. A successful microneedle should both penetrate grape leaf xylem without fracture and enable sufficient fluid transport of plant sap through its bore, without clogging. Nitrite sensors for plant nutrition logically could follow. Parallel fabrication and low device maintenance would ensure effective cost control.

## Fabrication:

After furnace deposition of silicon nitride ( $\text{Si}_3\text{N}_4$ ), the  $\text{Si}_3\text{N}_4$  on the backside of the wafer was patterned using contact lithography and etched to create an etch mask. The exposed silicon was then etched using 33% potassium hydroxide at 90°C for 35 minutes. This created a backside trench of 68  $\mu\text{m}$  deep (Figure 1). The presence of this trench reduced the time necessary to create a through hole in later inside-diameter etching. The trench also created a site for future pressure sensor placement. The next few steps in the process are shown in Figure 2. First, the annulus was patterned; 3  $\mu\text{m}$  of oxide was first deposited on the front side of the wafer using plasma enhanced chemical vapor deposition (PECVD).

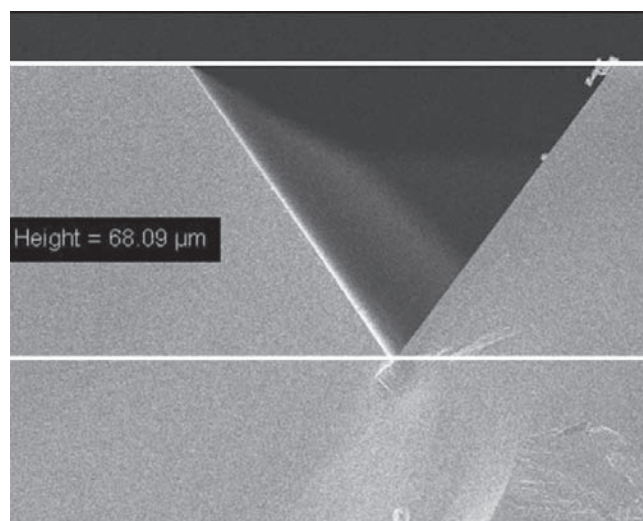


Figure 1: SEM of backside trench.

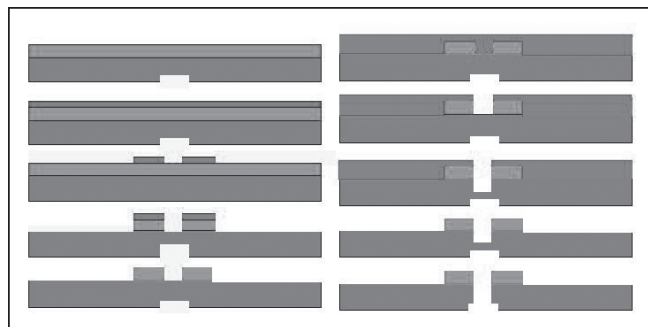


Figure 2: Process flow for needle fabrication.

This oxide was then patterned with contact lithography and etched using a 6:1 buffered oxide etch (BOE) for 35 minutes. The remaining oxide, after resist removal, served as silicon etch mask for the purpose of etching the annulus. Since only the inside diameter of the needle needed to be etched completely through the wafer (a longer etch time as opposed to the outside diameter etch duration), photoresist was applied and patterned in a manner such that only the inner diameter silicon was etched away. An initial 125  $\mu\text{m}$  was etched using the Oerlikon deep silicon etcher. Then, after removing the resist, etching was continued so that the entire wafer (except the annulus, masked with oxide) was etched. This process created the sidewalls and allowed for further inner diameter etching. Upon etch completion, needle lengths of 150 to 200  $\mu\text{m}$  were measured (Figure 3).

**Results and Discussion:**

Difficulties in boring completely through to the other side of the wafer were experienced. Further, in cases of sidewall thicknesses of less than 15  $\mu\text{m}$ , the elongated episodes of linear etching down the length of the needle shaft partially eroded through these sidewalls (Figure 4). This resulted in needle breakage. Thicker sidewalls did survive etching and their strength was tested.

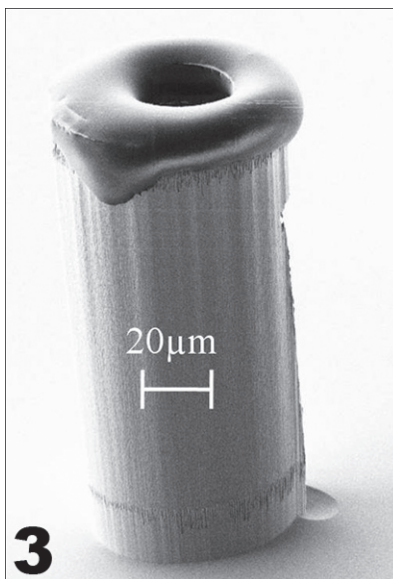


Figure 3: SEM of needle after etch completion.

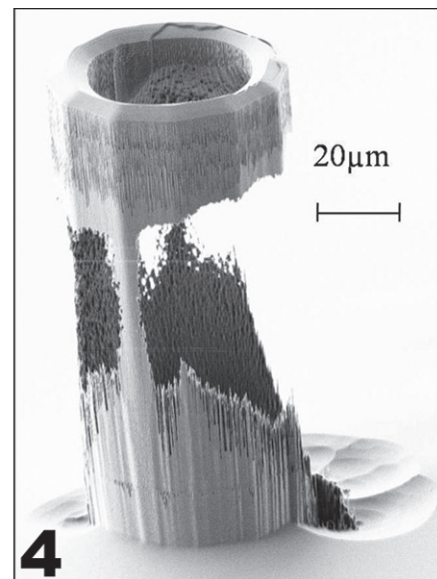


Figure 4: Sidewall damage on needles with sidewall thicknesses of less than 15  $\mu\text{m}$ .

For initial testing of these needles, in lab methods were used. A grape vine leaf was removed from the plant and pressurized to mimic the vacuum existing in plants. Microneedle insertion into the xylem was monitored via microscope. Insertion was successful with needles of 200  $\mu\text{m}$  length. Shorter needles drifted off location which resulted in breakage. The development of a single hollow microneedle requires further research and development. Longer etch times prior to resist removal could ensure through-hole success, and longer etches after resist removal (for needles with larger wall thicknesses) could generate longer needles. The fabrication of tapered versus parallel-walled needles should be explored. Ultimately, successful needle manufacture should be followed up with the installation of the water pressure sensor and nitrate sensor.

**Acknowledgements:**

I would like to thank the following organizations and people: National Nanotechnology Infrastructure Network Research Experience for Undergraduates (NNIN REU) Program; National Science Foundation; Cornell NanoScale Science & Technology Facility; CNF Staff especially Melanie-Claire Mallison; my PI: Abraham Stroock; my mentor: Amit Pharkya; Vinay Pagay, Peter J. Melcher, and CNF users: Stephen Jones and Nicolás Sherwood Droz.

**References:**

- [1] "Comparative measurements of xylem pressure in transpiring and non-transpiring leaves by means of the pressure chamber and the xylem pressure probe", P.J. Melcher et al., Journal of Experimental Botany, Vol.49, n°327, pp.1757-1760, October 1998.
- [2] "Microneedle array for transdermal biological fluid extraction and *in situ* analysis", E.V. Mukerjee et al., Sensors and actuators A, Physical, 2004, vol. 114, no2-3, pp. 267-275.

# Artificially-Manufactured Surface-Enhanced Raman Scattering-Active Nanoparticles for Cancer Diagnostics

Sweta Sengupta

Biology and Computer Science, Emory University

NNIN REU Site: Stanford Nanofabrication Facility, Stanford University, Stanford, CA

NNIN REU Principal Investigator(s): Dr. Shan Wang, Material Science and Electrical Engineering, Stanford Nanofabrication Facility, Stanford University, Stanford, CA

NNIN REU Mentor(s): Dr. Jung-Sub Wi, MSE, Stanford University; Dr. Robert Wilson, MSE, Stanford University; Dr. Mary Tang, Stanford Nanofabrication Facility, Stanford University

Contact: ssengu2@emory.edu, sxwang@stanford.edu

## Abstract:

Surface-enhanced Raman scattering (SERS) is a powerful method for examining biological samples. Antibody marked SERS-active nanoparticles can be used in human serum bioassays to detect cancer cells. In this report, we show preliminary results on artificially engineered SERS nanoparticles. These nanoparticles are designed for enhancing a local electromagnetic field and are fabricated by nanoimprint lithography, thin film deposition, and release of nanoparticles from substrate. Uniformly created nanoparticles and their enhanced Raman signals are confirmed by scanning electron microscope and Raman spectroscopy.

## Introduction:

Raman scattering, which is based on the energy shift by inelastic scattering between incident photons and molecules, has long been considered to have possible diagnostic advantages. Raman scattering produces a sharp spectrum, not susceptible to photobleaching, and maintains multiplexing capabilities.

Despite the advantages, Raman scattering is weak and nearly indistinguishable from background noise. However, with the advent of surface-enhanced Raman scattering (SERS), created from the adsorption of textured, aggregate, and/or structured nanometer sized metal nanoparticles to Raman dye, signal intensity of Raman scattering can be increased several folds, making Raman dyes a feasible option as labels in immunoassays.

For achieving this benefit, many research groups have been studying the enhanced Raman scattering from clustering of nanoparticles. However, reliability and controllability of aggregated nanoparticles with rough and irregular surfaces are still under investigation [1].

Here, we performed preliminary fabrication and assessments of the validity of artificially designed SERS nanoparticles and their potential to amplify Raman scattering. Our research idea was to create SERS nanoparticles with uniform size and shape by using nanoimprint lithography. These nanoparticles also could be functionalized with antibodies for bioassay purposes.

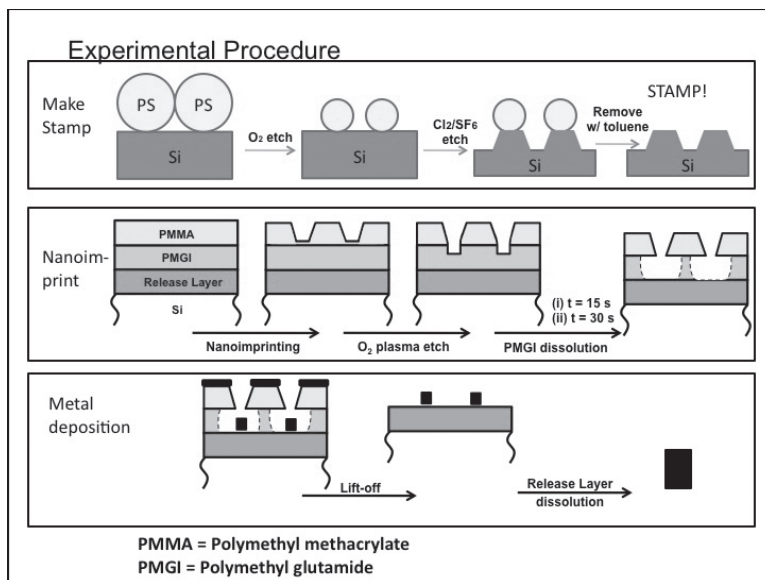
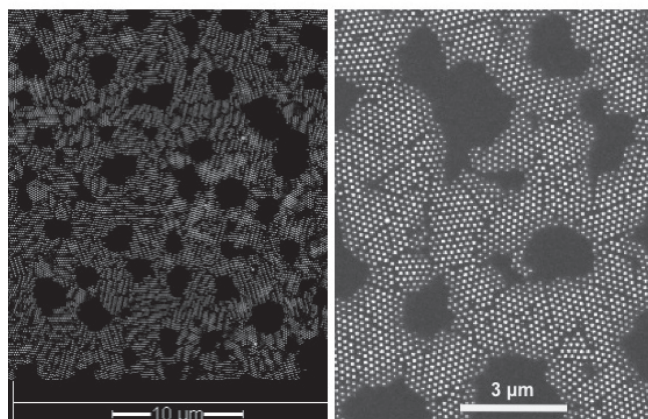


Figure 1: Nanoparticles were created using three steps: make a stamp, nanoimprint, and then metal deposition.

## Experimental Procedure:

At first, a nanoimprint stamp was created by selective plasma etching of a silicon (Si) substrate with spin coated polystyrene beads as an etching hard mask. Using the anisotropic oxygen ( $O_2$ ) plasma condition for reducing a size of polystyrene bead and anisotropic chlorine sulfur hexafluoride ( $Cl_2/SF_6$ ) plasma condition for vertical etching of Si substrate, the

## SEM of Ag Nanoparticles



nanoimprint stamp was fabricated. Once the stamp was created, nanoimprint lithography, O<sub>2</sub> plasma etching, PMGI dissolution, and silver (Ag) film deposition were carried out sequentially for creating Ag nanoparticles, as depicted in Figure 1. Ag nanoparticles were then submerged overnight in a methylene blue (Raman dye) solution. Scanning electron microscopy (SEM) and Raman spectroscopy were used to characterize the particles and assess the SERS, respectively.

### Results and Conclusions:

We were able to create a nanoimprint stamp with a 70 nm sized nano-dot array by studying and optimizing etching conditions for polystyrene and Si substrates. With this stamp, uniform Ag nanoparticles with 70 nm diameter and 30 nm thicknesses were successfully created (Figure 2). The preliminary Raman spectroscopy analysis demonstrated the presence of a huge Raman signal enhancing from the Ag nanoparticles. In addition, the Raman signal peak was uniform and reproducible (Figure 3).

### Future Work:

The next step will be to functionalize the SERS nanoparticle surface with various antibodies and examine biological samples (Figure 4). We will also investigate more techniques to enhance Raman scattering, including creating surface roughness and irregularities.

### Acknowledgements:

I would like to thank Jung-sub Wi, Bob Wilson, Maureen Baran, Edward Barnard, Mingliang Zhang, Mary Tang, Mike Deal, Shan Wang, and the National Nanotechnology Infrastructure Network Research Experience for Undergraduates (NNIN REU) Program.

### References:

- [1] K.Kneipp, M. Moskovits, H. Kneipp (Eds); Surface-Enhanced Raman Scattering- Physics and Applications. Topics Appl. Phys. 103, 409-426 (2006) Springer-Verlag Berlin Heidelberg, 409-424.

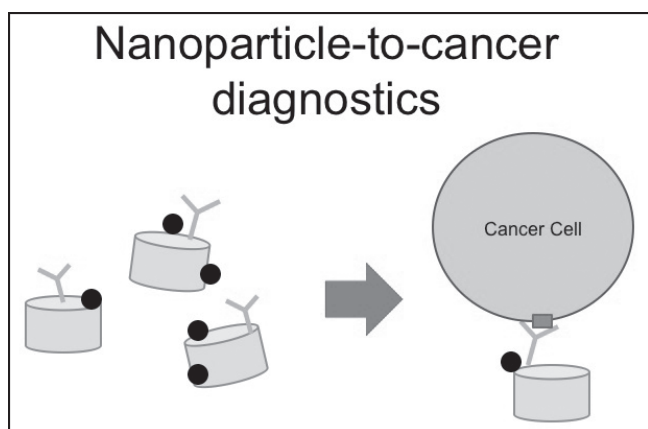
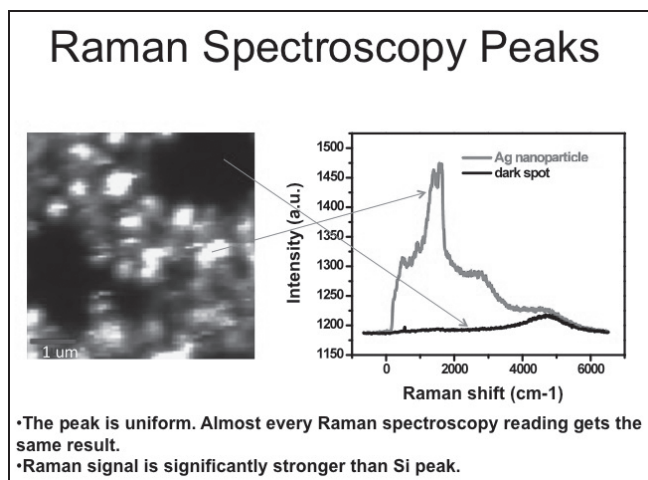


Figure 2, top: Plan view SEM images of unreleased 70 nm diameter Ag nanoparticles.

Figure 3, middle: The above Raman spectroscopy data demonstrates that the bright regions from the Raman intensity map (left) corresponds to the 1600~1700 cm<sup>-1</sup> Raman peak (right), which is characteristic of methylene blue. The Raman peak reading was also uniform and reproducible.

Figure 4, bottom: The diagram demonstrates how Ag nanoparticles with Raman dye (small circles) and antibodies (y-shaped structures) can localize to cancer cell markers.

# Development of a Multiplex CARS Flow Cytometer for Label-Free, Real-Time Classification

Hamsa Sridhar

Physics and Mathematics, Harvard College

**NNIN REU Site:** Nanotechnology Research Center, Georgia Institute of Technology, Atlanta, GA

**NNIN REU Principal Investigator(s):** Prof. Ali Adibi, Electrical and Computer Engineering, Georgia Tech

**NNIN REU Mentor(s):** Dr. Siva Yegnanarayanan, Charles Camp, Electrical and Computer Engr, Georgia Tech

**Contact:** [hsridhar@fas.harvard.edu](mailto:hsridhar@fas.harvard.edu), [adibi@ece.gatech.edu](mailto:adibi@ece.gatech.edu), [sivay@ece.gatech.edu](mailto:sivay@ece.gatech.edu), [ccampjr@ece.gatech.edu](mailto:ccampjr@ece.gatech.edu)

## Abstract:

An effective, label-free method of identifying unknown particles in a flow cytometer is presented through the application of multiplex coherent anti-Stokes Raman spectroscopy (MCARS) to a microfluidic chip. Various designs for microfluidic channels were theoretically modeled using COMSOL Multiphysics and fabricated using photolithography. A program was written in MATLAB to perform principal component analysis in order to determine the spectra of unknown substances and to classify them in real-time. As proof of principle, chemically specific differentiation of polystyrene microbeads and oil was experimentally demonstrated.

## Introduction:

Flow cytometers are used to observe and characterize individual microscopic particles, such as cells, in a stream of fluid. The major advantage of using these devices, as opposed to examining single droplets in a microscope, is the high throughput of sample in a given time frame. Current cytometers use laser scattering to classify cell size and shape, and fluorophores, which bind to specific proteins on the surface of a cell, for chemical identification. However, such endogenous fluorophores can disrupt the physiological systems of living samples. Moreover, it requires advance knowledge of the substances present. Additionally, the large fluorescence bandwidth renders multiplexing of multiple fluorophores challenging; it also requires hardware-intensive structures, including the use of several pump lasers at different wavelengths and unique sets of excitation/emission filters and photomultipliers (PMTs) for each multiplex channel. Hence, there is a need for chemically specific, label-free classification in a flow cytometer.

In this work, MCARS was applied to cytometric analysis on a microfluidic chip. Multiplex coherent anti-Stokes Raman scattering (MCARS) is a label-free method of optical imaging that uses the vibrational chemical signature of molecules to uniquely identify and visualize them. As a result, it eliminates the need for fluorophores. Moreover, the coherent pumping of Raman bands and multiplex detection allow for high sensitivity and full spectrum measurements (Figure 1). This new addition to flow cytometry complements traditional sizing and morphological information with fluorophore-free chemical information. Moreover, the narrow Raman spectral peaks, compared to the broad emissions from fluorophores, further facilitate multiplexing.

The aim of this project was to fabricate a MCARS cytometer that could effectively flow a mixture of various cells in a

stream of fluid, and analyze their chemical signatures in real-time, thereby allowing for down-stream sorting of the sample. (See Figure 1.)

**Microfluidic Design.** Fluid flow is governed by the Navier-Stoke equation. In microfluidics, flow speeds are approximately quartically proportional to the channel diameter. Therefore, microfluidic channels were designed to perform hydrodynamic focusing, a method of maintaining fast and thin sample flows by means of adding a sheath fluid. Such focusing was theoretically modeled in COMSOL Multiphysics through the Navier-Stokes incompressible flow and convection / diffusion modules (Figure 2). It was found through this form of analysis that for a 1000 psi pressure drop across the sample microfluidic channel, a volumetric flow rate of approximately 3 microliters per second could be achieved. This would allow the system to analyze approximately 30 to  $3 \times 10^5$  cells per second, depending on sample concentration

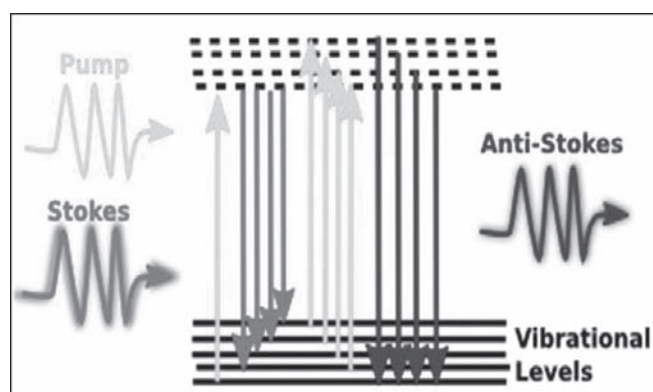


Figure 1: The energy-level diagram for MCARS is shown. The use of white light as the Stokes beam allows gathering of information about all the vibrational energy states of the molecule.

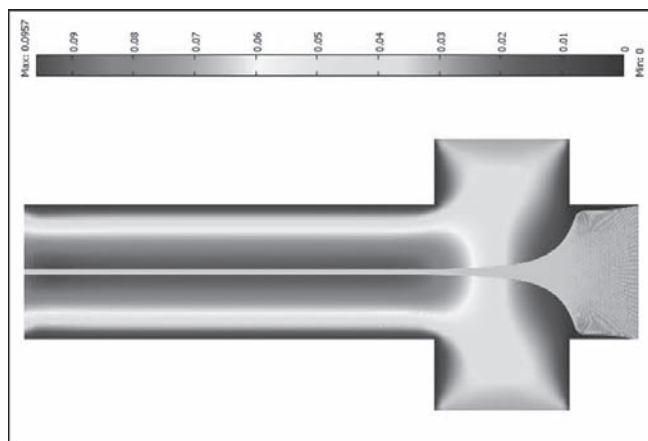


Figure 2: A COMSOL velocity field plot of hydrodynamic focusing is shown. The three inlet channels are all 150  $\mu\text{m}$  wide and the sample particles (represented by the grey streamlines) from the center inlet are focused into a thin stream by the sheath fluid.

and the CCD frame rates, which is comparable to current industry standards. Such a microfluidic channel design was chosen and drawn in Auto CAD, as shown in Figure 2.

**Fabrication.** Fabrication of the microfluidic channels was done through photolithography. A chrome mask of the channel designs was purchased from Photosciences, Inc. First, a 30  $\mu\text{m}$  layer of SU-8 (negative photoresist) was spun on a silicon wafer. A two-step bake was performed to cure the resist. Then, it was exposed to 365 nm UV light for 13 seconds and developed for 5 minutes. The prepared wafer was then coated with 100 nm of chrome and 200 nm of gold using electron-beam evaporation. Next, polydimethylsiloxane (PDMS) was prepared by mixing Sylgard 184 with its curing agent in a 10:1 ratio. The mixture was degassed under vacuum, poured uniformly onto the wafer, and cured for 4 hours at 70°C. Then, the PDMS layer was peeled off and holes were punched in it for attaching nanoports. Finally, the PDMS was treated with oxygen plasma for 10 seconds at 50W before sealing it to a glass slide, completing the fabrication process.

**Analysis.** In order to analyze the MCARS spectral data collected from these microfluidic devices, a chemometric tool called principal component analysis (PCA) was used. PCA is a mathematical method that decomposes data into an alternative basis, maximizing variance between subsequent principal components, or basis vectors. Each substance's spectrum can then be easily identified as linear combinations of the first few principal components.

A GUI was written in MATLAB to perform this analysis. First, it applied a Savitsky-Golay filter and normalized the data. Next, PCA was performed. Then, the projection of each spectra onto the first few principal components was graphed. This caused clustering which allowed one to differentiate and identify various substances. This method was used successfully to differentiate polystyrene beads in oil although the MCARS spectra of both substances are very similar (Figure 3).

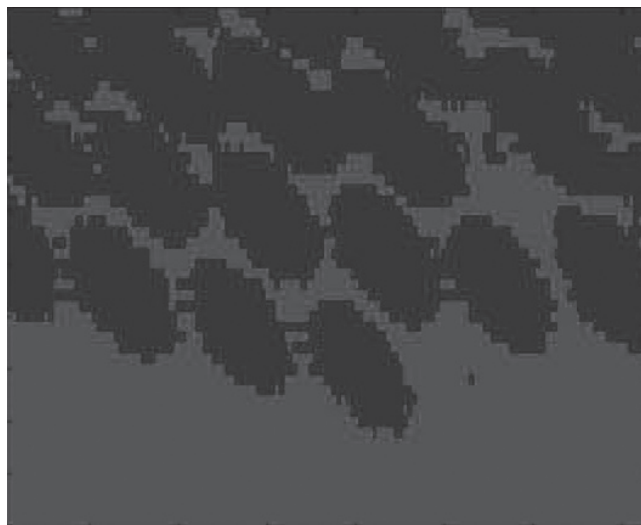


Figure 3: An image of polystyrene beads (black) in oil (grey) is shown. It was reconstructed in MATLAB by performing PCA on the MCARS spectral data collected.

Once the spectrum of each substance is determined through a training set, real-time identification can be implemented by grabbing one spectrum of a particle flowing by and matching it to the various spectra collected beforehand through the training set.

### **Conclusions:**

Microfluidic channels with the capacity for hydrodynamic focusing were modeled theoretically, designed, and fabricated. A program in MATLAB was written to differentiate and identify various substances flowing through the microfluidic devices by applying PCA to the spectral data collected. In this manner, chemically specific differentiation of polystyrene and oil was experimentally demonstrated. This sets the groundwork for the implementation of a flow cytometer chip that will perform real-time identification of particles using MCARS.

### **Future Work:**

Once real-time particle identification is accomplished, it will be useful to introduce a sorting device to classify the particles into bins accordingly. Common methods of doing this include the use of micro-actuators, magnetic coatings, or electric potentials. It is also beneficial to introduce cameras in order to determine the size of particles through scattered light.

### **Acknowledgments:**

I would like to thank the National Science Foundation (NSF), the NNIN REU Program, and the Georgia Institute of Technology for funding and providing facilities for conducting this research. Furthermore, I would like to extend my gratitude to Prof. Ali Adibi, Dr. Siva Yegnanarayanan, and Charles Camp for including me in their research and guiding me through this work.